Positron annihilation study of Al-Cu-Fe FCI quasicrystals

by

Derek W. Lawther

Submitted in partial fulfillment
of the requirements for the degree of
Doctor of Philosophy
at
Dalhousie University
Halifax, Nova Scotia, Canada
September, 1993

ISBN 0-315-93784-X

Name Derek. W. Lawther

Dissertation Abstracts International is arranged by broad, general subject categories Please select the one subject which most nearly describes the content of your dissertation Enter the corresponding four-digit code in the spaces provided

Physics · Solid State
SUBJECT TERM

0611
SUBJECT CODE

U·M·I

Subject Categories

THE HUMANITIES AND SOCIAL SCIENCES

COMMUNICATIONS AND THE ARTS
- Architecture 0729
- Art History 0377
- Cinema 0900
- Dance 0378
- Fine Arts 0357
- Information Science 0723
- Journalism 0391
- Library Science 0399
- Mass Communications 0708
- Music 0413
- Speech Communication 0459
- Theater 0465

EDUCATION
- General 0515
- Administration 0514
- Adult and Continuing 0516
- Agricultural 0517
- Art 0273
- Bilingual and Multicultural 0282
- Business 0688
- Community College 0275
- Curriculum and Instruction 0727
- Early Childhood 0518
- Elementary 0524
- Finance 0277
- Guidance and Counseling 0519
- Health 0680
- Higher 0745
- History of 0520
- Home Economics 0278
- Industrial 0521
- Language and Literature 0279
- Mathematics 0280
- Music 0522
- Philosophy of 0998
- Physical 0523
- Psychology 0525
- Reading 0535
- Religious 0527
- Sciences 0714
- Secondary 0533
- Social Sciences 0534
- Sociology of 0340
- Special 0529
- Teacher Training 0530
- Technology 0710
- Tests and Measurements 0288
- Vocational 0747

LANGUAGE, LITERATURE AND LINGUISTICS
- Language
  - General 0679
  - Ancient 0289
  - Linguistics 0290
  - Modern 0291
- Literature
  - General 0401
  - Classical 0294
  - Comparative 0295
  - Medieval 0297
  - Modern 0298
  - African 0316
  - American 0591
  - Asian 0305
  - Canadian (English) 0352
  - Canadian (French) 0355
  - English 0593
  - Germanic 0311
  - Latin American 0312
  - Middle Eastern 0315
  - Romance 0313
  - Slavic and East European 0314

PHILOSOPHY, RELIGION AND THEOLOGY
- Philosophy 0422
- Religion
  - General 0318
  - Biblical Studies 0321
  - Clergy 0319
  - History of 0320
  - Philosophy of 0322
- Theology 0469

SOCIAL SCIENCES
- American Studies 0323
- Anthropology
  - Archaeology 0324
  - Cultural 0326
  - Physical 0327
- Business Administration
  - General 0310
  - Accounting 0272
  - Banking 0770
  - Management 0454
  - Marketing 0338
- Canadian Studies 0385
- Economics
  - General 0501
  - Agricultural 0503
  - Commerce Business 0505
  - Finance 0508
  - History 0509
  - Labor 0510
  - Theory 0511
- Folklore 0358
- Geography 0366
- Gerontology 0351
- History
  - General 0578
  - Ancient 0579
  - Medieval 0581
  - Modern 0582
  - Black 0328
  - African 0331
  - Asia, Australia and Oceania 0332
  - Canadian 0334
  - European 0335
  - Latin American 0336
  - Middle Eastern 0333
  - United States 0337
- History of Science 0585
- Law 0398
- Political Science
  - General 0615
  - International Law and Relations 0616
  - Public Administration 0617
- Recreation 0814
- Social Work 0452
- Sociology
  - General 0626
  - Criminology and Penology 0627
  - Demography 0938
  - Ethnic and Racial Studies 0631
  - Individual and Family Studies 0628
  - Industrial and Labor Relations 0629
  - Public and Social Welfare 0630
  - Social Structure and Development 0700
  - Theory and Methods 0344
- Transportation 0709
- Urban and Regional Planning 0999
- Women's Studies 0453

THE SCIENCES AND ENGINEERING

BIOLOGICAL SCIENCES
- Agriculture
  - General 0473
  - Agronomy 0285
  - Animal Culture and Nutrition 0475
  - Animal Pathology 0476
  - Food Science and Technology 0359
  - Forestry and Wildlife 0478
  - Plant Culture 0479
  - Plant Pathology 0480
  - Plant Physiology 0817
  - Range Management 0777
  - Wood Technology 0746
- Biology
  - General 0306
  - Anatomy 0287
  - Biostatistics 0308
  - Botany 0309
  - Cell 0379
  - Ecology 0329
  - Entomology 0353
  - Genetics 0369
  - Limnology 0793
  - Microbiology 0410
  - Molecular 0307
  - Neuroscience 0317
  - Oceanography 0416
  - Physiology 0433
  - Radiation 0821
  - Veterinary Science 0778
  - Zoology 0472
- Biophysics
  - General 0786
  - Medical 0760

EARTH SCIENCES
- Biogeochemistry 0425
- Geochemistry 0996
- Geodesy 0370
- Geology 0372
- Geophysics 0373
- Hydrology 0388
- Mineralogy 0411
- Paleobotany 0345
- Paleoecology 0426
- Paleontology 0418
- Paleozoology 0985
- Palynology 0427
- Physical Geography 0368
- Physical Oceanography 0415

HEALTH AND ENVIRONMENTAL SCIENCES
- Environmental Sciences 0768
- Health Sciences
  - General 0566
  - Audiology 0300
  - Chemotherapy 0992
  - Dentistry 0567
  - Education 0350
  - Hospital Management 0769
  - Human Development 0758
  - Immunology 0982
  - Medicine and Surgery 0564
  - Mental Health 0347
  - Nursing 0569
  - Nutrition 0570
  - Obstetrics and Gynecology 0380
  - Occupational Health and Therapy 0354
  - Ophthalmology 0381
  - Pathology 0571
  - Pharmacology 0419
  - Pharmacy 0572
  - Physical Therapy 0382
  - Public Health 0573
  - Radiology 0574
  - Recreation 0575
  - Speech Pathology 0460
  - Toxicology 0383
- Home Economics 0386

PHYSICAL SCIENCES

Pure Sciences
- Chemistry
  - General 0485
  - Agricultural 0749
  - Analytical 0486
  - Biochemistry 0487
  - Inorganic 0488
  - Nuclear 0738
  - Organic 0490
  - Pharmaceutical 0491
  - Physical 0494
  - Polymer 0495
  - Radiation 0754
- Mathematics 0405
- Physics
  - General 0605
  - Acoustics 0986
  - Astronomy and Astrophysics 0606
  - Atmospheric Science 0608
  - Atomic 0748
  - Electronics and Electricity 0607
  - Elementary Particles and High Energy 0798
  - Fluid and Plasma 0759
  - Molecular 0609
  - Nuclear 0610
  - Optics 0752
  - Radiation 0756
  - Solid State 0611
- Statistics 0463

Applied Sciences
- Applied Mechanics 0346
- Computer Science 0984
- Engineering
  - General 0537
  - Aerospace 0538
  - Agricultural 0539
  - Automotive 0540
  - Biomedical 0541
  - Chemical 0542
  - Civil 0543
  - Electronics and Electrical 0544
  - Heat and Thermodynamics 0348
  - Hydraulic 0545
  - Industrial 0546
  - Marine 0547
  - Materials Science 0794
  - Mechanical 0548
  - Metallurgy 0743
  - Mining 0551
  - Nuclear 0552
  - Packaging 0549
  - Petroleum 0765
  - Sanitary and Municipal 0554
  - System Science 0790
- Geotechnology 0428
- Operations Research 0796
- Plastics Technology 0795
- Textile Technology 0994

PSYCHOLOGY
- General 0621
- Behavioral 0384
- Clinical 0622
- Developmental 0620
- Experimental 0623
- Industrial 0624
- Personality 0625
- Physiological 0989
- Psychobiology 0349
- Psychometrics 0632
- Social 0451

Contents

List of Figures

List of Tables

Abstract

Three positron annihilation techniques have been employed for the study of defect formation and behavior in Al-Cu-Fe face centered icosahedral (FCI) quasicrystals. Room temperature Doppler broadening and positron lifetime techniques were used to study the samples as a function of thermal treatment. An *in situ* Doppler broadening technique was used to study the samples at elevated temperatures.

Results from measurements on sample stoichiometries of $Al_{63}Cu_{25}Fe_{12}$, $Al_{62.5}Cu_{25}$-$Fe_{12.5}$, $Al_{62}Cu_{25.5}Fe_{12.5}$ and $Al_{62}Cu_{22.5}Fe_{15.2}$ are reported.

Quenched-in disorder has been observed in the samples. Reversion to the equilibrium behavior occurs after annealing the samples at 200°C.

Equilibrium vacancy formation and behavior has been observed and correlated with results from a variety of other techniques which have been reported in the literature.

A quasicrystal-to-microcrystal phase transition has been observed in two of the samples ($Al_{63}Cu_{25}Fe_{12}$ and $Al_{62}Cu_{22.5}Fe_{15.2}$), indicating an instability of the FCI phase at low temperatures. The FCI phase in the other two samples ($Al_{62.5}Cu_{25}Fe_{12.5}$ and $Al_{62}Cu_{25.5}Fe_{12.5}$) has been found to be stable over the entire temperature range investigated.

It is shown that intrinsic structural vacancies exist in both the microcrystal and FCI phases. The structural vacancy is interpreted in terms of an atomic structural unit in which an inner close-packed icosahedral shell of Al atoms surrounds a vacant central site.

Thermal activation of dynamic phason hopping has been observed in the FCI phase. At ~200°C, distortion of the intrinsic structural vacancies occurs as Al atoms of the inner icosahedral shell begin to hop within their double well potential. At higher temperatures (525°C-750°C depending upon the sample stoichiometry) Cu atom phason hopping is activated and is found to coincide with the onset of plasticity in the FCI phase.

List of Symbols

$\mathbf{a}_i$ - basis vector
$\mathbf{A}$ - atomic surface
ACAR - angular correlation of annihilation radiation
ADC - analog-to-digital converter
a_B - Bohr's radius
$\mathcal{A}$ - activity
$\mathcal{B}_i$ - channel background counts
CFDD - constant fraction differential discriminator
c - concentration
c_z - discrete Fourier component
$C_i^{2\gamma}$ - spectrum channel counts
DB - Doppler broadening
DT - electronic dead time
DUSR - Dalhousie university SLOWPOKE-2 reactor
erf - error function
E_o - electron rest energy
ϵ - γ-ray energy
ϵ_F - Fermi energy
ϵ_{max} - maximum energy of emitted positron
ϵ_γ - energy of fiducial γ-ray
e/a - electrons per atom
F - Doppler broadening lineshape parameter
f_z - discrete Fourier component
FCI - face centered icosahedral
FWHM - full width at half maximum
$\mathcal{F}_i$ - channel noise contribution
Φ - neutron flux
$\mathbf{G}$ - reciprocal lattice vector
$\gamma_{positron}$ - γ-rays per positron emission

H_v - enthalpy of vancancy formation
HPGe - high purity germanium
HREM - high resolution electron microscopy
HV - high voltage
I - intensity
I_p - intensity of parabolic component
k_B - Boltzmann constant
k_F - Fermi wavevector
κ - positron trapping rate
L - positron lifetime measurement
L - Doppler broadening lineshape parameter
λ - annihilation rate
m - mass
m_o - electron rest mass
$\mathcal{M}_i$ - channel multiplication factor
MCA - multichannel analyser
μ - specific positron-trapping rate
N - vacancy size
N_{decay} - positrons emitted per decay
$N.A.$ - natural abundance
n_a - atomic density
n_e - electron density
ω - angular frequency
Ω - rate of change of source/detector separation
PMT - photomultiplier tube
p_z - discrete Fourier component
$\mathcal{P}^{2\gamma}(\varepsilon)$ - energy distribution
r_z - discrete Fourier component
$\mathcal{R}$ - resolution function
ρ - resistivity
$\mathbf{R}$ - physical space
$\rho(\mathbf{r})$ - atomic mass density
S - Doppler broadening lineshape parameter
s_v - entropy of vacancy formation

SI - simple icosahedral

σ - electrical conductivity

σ_c - thermal neutron cross section

TAC - time-to-analog converter

T - temperature

T_a - anneal temperature

t - time

$t_{1/2}$ - half-life

τ - positron lifetime

$\mathbf{v}$ - velocity

V - volume

VOF - variance-of-fit

W - Doppler broadening lineshape parameter

χ - susceptability

χ^2 - goodness-of-fit parameter

Acknowledgements

First and foremost I wish to express my sincere appreciation to my thesis supervisor, Professor R.A. Dunlap, for his guidance and unwaivering commitment to promoting the best interests of his students. This accolade is given not simply because it is the "politically correct" thing to do, but because it is in every sense a factual statement.

The experimental work reported on in this thesis was obtained primarily with equipment on loan from Dr. I.K. MacKenzie at the University of Guelph. His kindness and generosity in this matter, along with the benefits of his correspondences, have contributed significantly toward the successful completion of this work. I wish very much to express my gratitude to him.

Thanks also to J. Holzbecher and his staff at the DUSR facility for their assistance in performing the neutron irradiations of the samples.

Finally, I wish to acknowledge the valuable day-to-day interactions with fellow graduate students, Stephen P. Ritcey and Mammo Tewondwossen, and post-doctoral fellows, Drs. Z. Wang and Z.J. Yang.

During the course of this work, financal support was provided by the Natural Sciences and Engineering Research Council of Canada, the Isaac Walton Killiam foundation and the Walter C. Sumner foundation.

1 Introduction

Since the initial discovery in 1984 of a metastable quasicrystalline phase in rapidly quenched Al-transition metal alloys [1], quasicrystals have become, perhaps, the most thoroughly studied class of intermetallic compounds (see e.g. [2,3,4,5,6,7,8]). The defining characteristic of this ever growing class of materials (see Table 1.1) is the unique combination of long-range quasiperiodic positional order and long-range bond-orientational order with a *disallowed* crystallographic rotational symmetry. The most studied subgroup to date is the icosahedral quasicrystals (see Figure 1.1), so-called because their diffraction patterns possess the rotational point group symmetries of the icosahedron (decagonal, octagonal and dodecagonal quasicrystals have also been observed). This subgroup can be further divided into the simple icosahedral (SI) and face centered icosahedral (FCI) quasicrystals [1]. The former encompasses the earliest discovered quasicrystals which tend to be highly disordered and metastable. The FCI quasicrystals, on the other hand, can typically be prepared with minimal disorder and, in some cases, have been shown to be thermodynamically stable (e.g. Al-Cu-Fe and Al-Cu-Ru).

Subsequent investigations of these FCI quasicrystals have recently revealed the following physical properties to be inherent to these materials (for more extensive reviews see e.g. [2,6,8,54]).

1. Enhanced mechanical properties (hardness and brittleness [55]) compared to conventional crystalline alloys but with a brittle-to-plastic transition at an ele-

[1]Structures possessing higher than cubic symmetry necessarily require nonorthogonal basis vectors for complete indexing in three dimensions (3D). In the case of icosahedral symmetry, these basis vectors would correspond to six (non-collinear) vectors pointing from the center to the vertices of an icosahedron. In such cases, it is customary to view the structure in the higher dimensional space (in this case 6D) to ensure orthogonality of the basis set. For SI quasicrystals, the 6D hypercubic lattice is simple (each n_i,i=1,..6 index may take on any integer value) whereas for FCI quasicrystals, it is face centered (n_i all even or all odd).

Alloy system	Stable composition	Ref
	** *octagonal* **	
A-Ni-Si (A=V,Cr)	-	[9]
Mn-Si-(Al,Fe)	-	[10,11,12]
	** *decagonal* **	
Al-A (A=Ir,Pd,Pt,Os,Ru,Rh)	-	[12,13,14,15]
Al-A-(Si,Ge) (A=Mn,Fe,Co,Ni,Cr)	-	[14,16,17,18,19,20]
Al-Mn-Fe	-	[21]
Al-Cu-A (A=Mn,Fe,Co,Ni)	$Al_{65}Cu_{20}Co_{15}$	[22,23]
V-Ni-Si	-	[18]
Al-Co-A (A=Fe,Ni)	$Al_{70}Co_{15}Ni_{15}$	[24,25]
Al-Pd-Fe	$Al_{75}Pd_{15}Fe_{10}$	[26]
Al-Pd-Mn	$Al_{70}Pd_{13}Mn_{17}$	[27]
	** *dodecagonal* **	
Cr-Ni	-	[28]
V-Ni(Si)	-	[29]
	** *simple icosahedral (SI)* **	
Al-A(Si,Ge) (A=Mn,Fe,Cr,V,Mo,W)	-	[1,15,30,31,32]
Al-A(Si,Ge) (A=Ru,Re)	-	[33,34]
Al-Fe-A (A=V,Cr,Mn)	-	[35]
Al-Li-A (A=Cu,Au,Zn)	$Al_{60}Cu_{10}Li_{30}$	[32,36]
Al-Cu-Mg	-	[37]
Ti-A(Si) (A=V,Mn,Fe,Co,Ni)	-	[38,39,40]
Mg-A (A=Al,Zn,Cu)	-	[41,42]
Fe-A (A=Cu,Nb)	-	[14]
Ni-A(Si) (A=Mn,Cu,Zr)	-	[43]
Mo-Fe-Cr-Si	-	[44]
Pd-U-Si	-	[45]
Ga-Mg-Zn	$Ga_{16}Mg_{32}Zn_{52}$	[46]
	** *face centered icosahedral (FCI)* **	
Al-Cu-A(B) (A=Mn,V)	-	[47,48,49]
Al-Cu-A (A=Fe,Cr,Ru,Os)	$Al_{65}Cu_{20}A_{15}$	[48,50,51]
Al-Pd-A(B) (A=Mn,Re)	$Al_{70}Pd_{20}A_{10}$	[49,52]

Table 1.1: Classification of the known quasicrystal-forming alloys as of the time of preparation of this thesis.

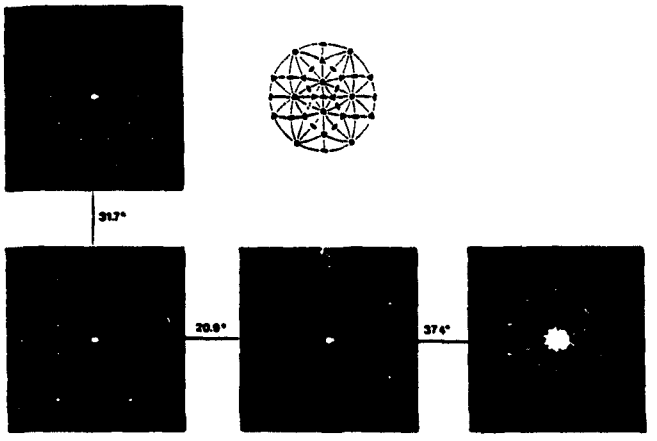

(a)

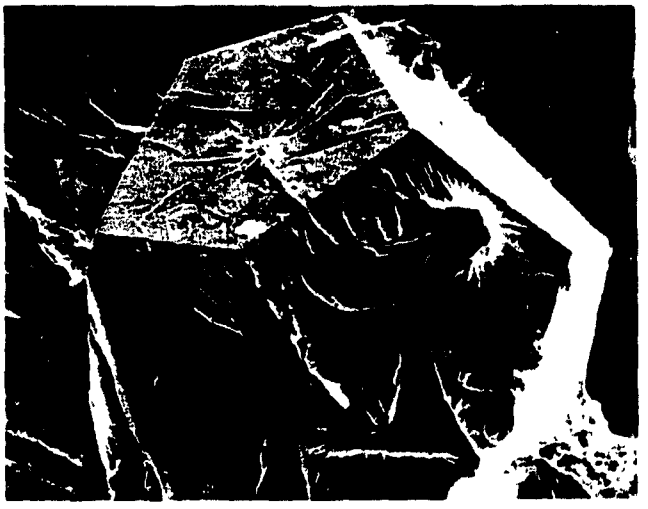

(b)

Figure 1.1: (a) Diffraction patterns of an icosahedral quasicrystal and (b) the dodecahedral grain shape observed in an Al-Cu-Fe FCI quasicrystal. Also shown are the relative orientations of various symmetry axes.
(Adapted from Figure 2.16 of [6] and Figure 5.2 of [53])

vated temperature [55,56,57].

2. High resistivities ($\sim$10000$\mu\Omega$·cm) with a pronounced negative temperature coefficient ($\rho_{4.2K}/\rho_{300K} \simeq 2$). Both effects are enhanced as the structural quality increases [58,59]. The corresponding conductivities fall well below Mott's minimal metallic limit and calculation of the mean free path assuming a spherical Fermi surface and free electrons yields the unphysically low value of $\sim$0.1Å.

3. Low density of states at the Fermi energy as indicated by specific heat [54,60], soft x-ray emission and photoabsorption [61] measurements.

4. Weakly paramagnetic behavior in disordered quasicrystalline samples gives way to diamagnetic behavior ($\chi(4.2K)$ $\sim$-4x10^{-7}emu/g) in well ordered samples [58].

5. Quasicrystalline phase occurrence and stability very sensitive to stoichiometry and well correlated with a specific number of conduction electrons per atom, e/a [62].

The anomalous transport properties most certainly indicate the importance of a band structure effect similar to the more familiar Hume-Rothery stabilization mechanism [63] observed in conventional metallic alloys. The essential difference is that the consequences of such an effect are optimized in the quasicrystals. This follows from the high multiplicity (42 in the case of icosahedral symmetry) of the reciprocal lattice vectors allowing for a better match between the Fermi sphere and the corresponding set of Bragg planes [64].

However, a more thorough understanding of the physical properties of quasicrystals will no doubt require a firm understanding of the possible disorder which can be generated in these materials. As in the case of conventional ordered structures (i.e. crystalline), vacancies, dislocations and phonons are expected to form in quasicrystals although the added complexity of the underlying aperiodic lattice lead to some important differences in their behaviour and in at least one case leads to a unique form

of disorder (phasons). It was with this in mind that an investigation of the defect structures in quasicrystals was performed using the positron annihilation techniques and is reported on in this thesis.

The positron has been used to image the electron momentum (energy) distribution in the solid state for over forty years (a positronic calendar for the solid state can be found in [65]). However, the high affinity for the positron to localize within open volume defects remained unimagined until the mid 1960's. At that time, Brandt had formulated the plausible trapping of positrons in alkali halides [66] and in 1967 MacKenzie *et. al.* at Dalhousie obtained the first experimental evidence for positron localization at thermally generated monovacancies in elemental metals [67]. This was followed two years later by a successful theory of positron trapping in metals (see e.g. [68,69]). Unfortunately, when MacKenzie left Dalhousie in the late sixties so too did the positron research effort.

The material reported in this thesis is tantamount to a rebirth of the positron annihilation effort at Dalhousie University. This renewed interest is justified given the unique advantage offered to us by the close proximity of the SLOWPOKE-2 thermal neutron facility. Short irradiations of samples containing Cu (> few tenths of an atomic percent) result in the production of the positron emitting isotope, ^{64}Cu, with sufficient activity to carry out the annihilation experiments (the advantages of producing the positron source as an integral part of the sample as opposed to the conventional remote source or deposited source will be discussed in the chapter on experimental details). This is of particular relevance to the study of quasicrystals for which the majority of the best quality (in terms of structural order and stability) examples possess 20-25at% Cu (see Table 1.1).

The remainder of this thesis is organized as follows. In chapter 2, the physics of disorder in quasicrystals is surveyed and correlated with the various proposed atomic structural models. Emphasis is placed upon the prediction of structures which can be imaged by the positron annihilation techniques. In chapter 3, experimental details are given including a description of the data analysis procedures. Chapter 4 is a review

of the positron annihilation results on quasicrystals which have previously appeared in the literature. Chapter 5 reports experimental results from positron annihilation measurements on Al-Cu-Fe quasicrystals. Chapter 6 concludes the thesis with a discussion of future directions for the research.

2 Defects in quasicrystals

2.1 Introduction

Early speculation that quasicrystals might be inherently disordered and metastable was dispelled with the discovery of thermodynamically stable SI (Al-Cu-Li), FCI (Al-Cu-Fe, Al-Cu-Ru, etc.) and decagonal (Al-Cu-Co(Si)) phases. Indeed, these new quasicrystals possess translational correlation lengths and facetting morphology (with icosahedral symmetry) which rival the best conventional metallic crystals (see Figure 1.1(b)). As a result, it is now possible to observe the presence and behavior of defect structures characteristic of these novel phases without the hinderance of extrinsic defects produced by the non-equilibrium processing techniques (which are required to prepare the metastable phases).

The remainder of this chapter is devoted to a description of the types of disorder which are expected to be present in real quasicrystals. In particular, a novel form of disorder, called phasons, is introduced as a consequence of the quasiperiodicity of these materials. Through the use of a hyperspace construction (section 2.2), it is shown that the degree of phason disorder leads in a natural way to a classification of real quasicrystalline and closely related crystalline phases (section 2.3). Finally, the possible occurrence of the more familiar types of open volume defects (i.e. vacancies and dislocations) which are candidates for positron traps is discussed in section 2.4.

2.2 Hyperspace construction

The translational (quasiperiodic) order of quasicrystals implies that the Fourier transform of the atomic mass density can be expressed as a Fourier series,

$$\rho(\mathbf{r}) = \frac{1}{V}\sum_{\mathbf{G}} \rho(\mathbf{G}) exp(i\mathbf{G}\cdot\mathbf{r}) \tag{2.1}$$

just as in the case of an ordinary crystal. However, the high point symmetry (e.g. icosahedral) of the resulting reciprocal lattice requires that the number of integer linearly independent basis vectors, $\mathbf{a}_i$, needed to span it will exceed the spatial dimension. For example, six basis vectors pointing toward the vertices of an icosahedron are required to span the reciprocal lattice for the icosahedral quasicrystal,

$$\mathbf{G} = \sum_{i=1}^{6} n_i \mathbf{a}_i. \tag{2.2}$$

In cubic coordinates, the $\mathbf{a}_i$ are permutations of the form $(\pm 1, \pm\tau, 0)$ [1] and

$$\mathbf{G} = \sum_{i=1}^{3} (h_i + \tau k_i)\mathbf{a}_i \tag{2.3}$$

where h_i and k_i are integers.

The irrationality of τ leads to two unusual properties compared to a regular crystal.

1. The fractional parts of the quantities, $h_i + \tau k_i$, densely fill the interval [0,1]. The G vectors thus form a dense set of Bragg peaks in the reciprocal space.

2. As a consequence of (1), there is no smallest basic G-value.

Alternatively, the dense 3D reciprocal lattice can be represented as a periodic image in a higher dimensional space. For instance, equation 2.2 can be considered as a 6D periodic reciprocal lattice whose Fourier transform would generate a 6D periodic mass density distribution. This is the basis of the so-called *hyperspace construction* [70,71,72]. The physical 3D description is then produced by an appropriately oriented cut [2] and projection operation from the 6D image.

[1] $\tau = (1+\sqrt{5})/2 = 2\cos 36^\circ = 1.618034...$ is an irrational number commonly referred to as the *golden mean.*

[2] The hyperspace construction formalism works equally well for both quasiperiodic and periodic structures. In the case of a periodic structure, a rational cut (slope) through the hyperspace is used whereas in the case of a quasiperiodic structure, an irrational cut is used.

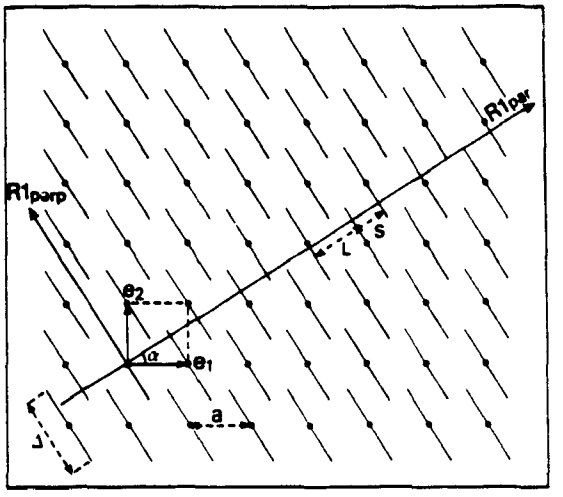

Figure 2.1: A 1D quasiperiodic chain (sequence of long, L, and short, S, segments) generated by a 1D irrational cut (at the angle, α) of a decorated 2D square lattice. Δ defines the atomic surface, $\mathbf{A}_{perp}$.
(Adapted from Figure 2 of [73])

This procedure is most readily envisioned in the analogous 2D hyperspace from which a 1D chain can be generated. Suppose that a 2D square lattice spans the hyperspace and the 1D physical (also referred to as parallel) space, $\mathbf{R1}_{par}$, is represented by a line which cuts through it. This is illustrated in Figure 2.1.

In general, the hyperspace lattice points are decorated with an atomic surface, $\mathbf{A}_{perp}$, the dimensionality of which corresponds to that of the complimentary perpendicular or phase space, $\mathbf{R}_{perp}$. In the case of the 2D hyperspace and 1D physical space, $\mathbf{R}_{perp}$ would have a dimension of one (in the case of a 3D quasicrystal, the hyperspace would have a dimension of six and $\mathbf{R}_{perp}$ a dimension of three).

These atomic surfaces must obey several criterion.

1. Projection of the $\mathbf{A}_{perp}$ into $\mathbf{R}_{par}$ generates the point-like atoms of the structure. Thus the atomic surfaces must have zero thickness in $\mathbf{R}_{par}$. In Figure 2.1 $\mathbf{A1}_{perp}$ is represented by a line segment parallel to $\mathbf{R1}_{perp}$.

2. $\mathbf{A}_{perp}$ must possess the symmetry of the structure (e.g. icosahedral).

3. A hard core condition applies; i.e. the $\mathbf{A}_{perp}$ must not intercept nor be closer to each other than the minimum physical separation parallel to $\mathbf{R}_{par}$. In Figure 2.1 the $\mathbf{A1}_{perp}$ are represented by finite line segments. They contribute as atomic positions in $\mathbf{R1}_{par}$ only if they intersect it.

4. Translational invariance must apply parallel to both $\mathbf{R}_{par}$ and $\mathbf{R}_{perp}$. It is the relative orientation of $\mathbf{R}_{par}$ which defines the structure, not the origin of $\mathbf{R}_{par}$.

2.3 Real quasicrystals: phason disorder

The hyperspace construction leads in a natural way to a description of both *phonon* disorder and *phason* disorder. The former is observed in both crystals and quasicrystals whereas the latter is unique to quasicrystals. Phonon disorder corresponds to a relative displacement of the individual atomic positions and this can be achieved by a displacement of the atomic surfaces parallel to $\mathbf{R}_{par}$. Conversely, the phason disorder results from a relative displacement of the atomic surfaces parallel to $\mathbf{R}_{perp}$, or equivalently, a translation of $\mathbf{R}_{par}$ along a $\mathbf{R}_{perp}$ direction. Recall that for a quasicrystal, the $\mathbf{A}_{perp}$ are discontinuous and the atomic positions are defined by the intersection of these $\mathbf{A}_{perp}$ with $\mathbf{R}_{par}$. Such a translation will necessarily result in atomic jumps (see Figure 2.1) or phasons. Note that in the case of a crystalline structure (i.e. a rational cut of the hyperspace), no such atomic jumps occur. Instead, the translation will at most result in a linear translation of the lattice.

There are two important distinctions between phonon and phason strain fields.

1. Since phason strains may involve discontinuous atomic jumps, they can be frozen into the structure if $k_B T$ is not sufficient to overcome the phason 'hop' energy barrier. Other properties such as relaxation time and response to applied stress may also be effected.

2. Like phonon strain, phason strain can distort the position, intensity (Debye-Waller) and shape of the resulting diffraction peaks. However, whereas the phonon strain effects scale with the physical scattering vector $\mathbf{G}_{par}$, the phason strain effects scale with $\mathbf{G}_{perp}$. For example, a conventional phonon strain will produce peak broadening which increases monotonically with $\mathbf{G}_{par}$ while phason strain will produce broadening which increases monotonically with $\mathbf{G}_{perp}$.

A classification of real quasicrystalline structures can be made based upon the nature of the displacement of $\mathbf{R}_{par}$ along $\mathbf{R}_{perp}$ (i.e. the phason strain field). The possible behaviors are illustrated in Figure 2.2 and summarized below.

1. No phason disorder results in a perfect quasicrystalline structure (Figure 2.2(a)). Possible candidates for this structure are FCI Al-Cu-Fe, Al-Cu-Ru, Al-Pd-Mn and decagonal Al-Cu-Co.

2. A linear strain can displace the orientation of $\mathbf{R}_{par}$ such that it becomes rational with respect to the hyperspace lattice. The resulting structure is said to be a crystalline (periodic) approximant to the perfect quasicrystalline structure (see Figure 2.2(b)).

3. Random fluctuations will induce positional disorder in $\mathbf{R}_{par}$. If these random phason strains are produced by bounded fluctuations (see Figure 2.2(c)), then the average orientation of the cut will remain irrational and a mean quasiperiodic structure will be maintained. However, the Bragg peaks will be attenuated (Debye-Waller factor) and a diffuse scattering component will appear in the diffraction spectra. This is the basis of the so-called *random tiling* model [74] which has gained some favour since it justifies the stability of the quasicrystalline phase through entropic reasons. A possible candidate for this structure is the SI Al-Cu-Li quasicrystal.

4. Unbounded random fluctuations (see Figure 2.2(d)) destroy the translational order of the structure and result in considerable broadening of the diffraction

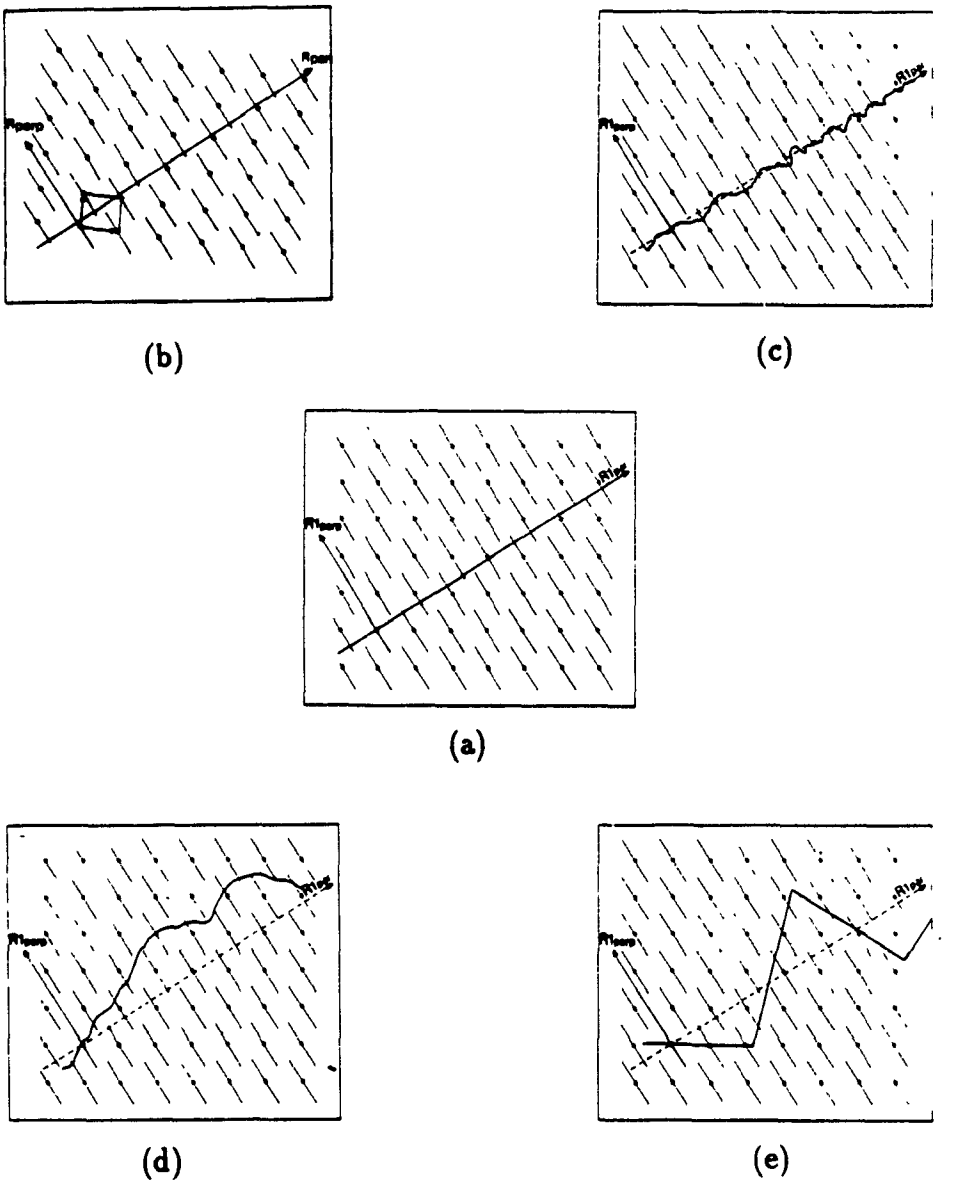

Figure 2.2: Examples of phason disorders generated by a 1D cut from a 2D hyperspace: (a) zero phason strain - perfect quasicrystal; (b) linear phason strain - crystalline (rational) approximant; (c) bounded random fluctuations - random tiling with average quasiperiodic order (diffuse scattering and attenuated Bragg peaks); (d) unbounded fluctuations and discontinuous tears - icosahedral glass (broad peaks with various shapes); and (e) rational facetting - microcrystal.

peaks which scales monotonically with $\mathbf{R}_{perp}$. This is the basis of the so-called *icosahedral glass model* [75] for which the metastable SI quasicrystals are candidates.

5. Anisotropic fluctuations destroy the average local orientation, breaking the icosahedral symmetry and shifting the diffraction peaks. In the special case of rational facetting of the orientation (see Figure 2.2(e)), local crystalline domains form resulting in a *microcrystalline* phase.

2.4 Positron traps in quasicrystals

Defects such as vacancies (point defects) and dislocations (line defects) have been shown to localize the positron prior to annihilation, allowing for an enhanced sensitivity of the positron annihilation techniques to their study. It is therefore of interest to know whether or not analogous defects can be expected to form in a quasicrystalline structure and in which ways (if any) their behavior may be expected to differ from their counterparts in conventional crystals.

In the case of quasicrystals, a distinction should be made between *intrinsic* and *extrinsic* vacancies. Intrinsic vacancies are expected to form in the quasicrystals due to their close relationship to crystalline approximant phases (as shown in the previous section). To date, many such approximants to the observed quasicrystalline phases have been observed [7], reaffirming this fact. A key feature of this closeness is the belief that they both posssess, more or less, the same local atomic structure. For example, α-Al-Mn-Si and R-Al-Cu-Li are known crystalline structures which also happen to be approximants to the Al-Mn-Si and Al-Cu-Li SI quasicrystals. Both of these crystals can be described as a bcc packing of atomic clusters with icosahedral symmetry (see Figure 2.3). Presumably, the corresponding quasicrystalline phases possess an alternative (aperiodic) packing of these same clusters (allowing for possible distortion). As Figure 2.3 shows, the central site of these two clusters is vacant and thus offers an ideal positron trap.

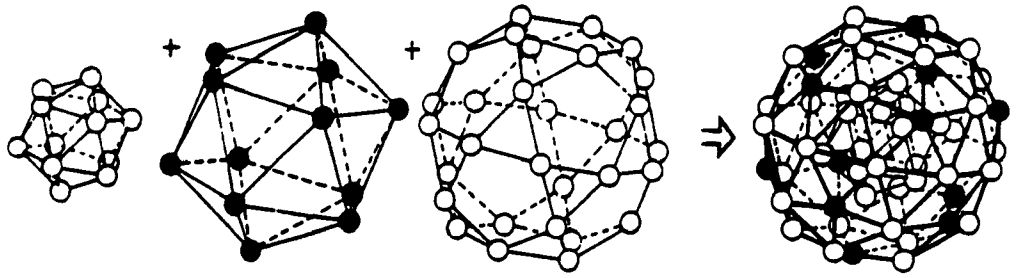

(a)

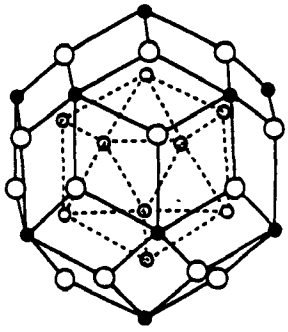

(b)

Figure 2.3: Atomic clusters with icosahedral symmetry found in cubic approximants: (a) 54-atom Mackay icosahedron of α-Al-Mn-Si; and (b) 44-atom Pauling triacontahedron of R-Al-Cu-Li. Note that the central icosahedral sites are vacant.

In addition, the incompatibility of the icosahedral symmetry of the atomic clusters with space-filling leads to the existence of 'gaps' (frustration) between them. Thus additional atoms, called *glue* atoms are required to fill these gaps. Interpenetration of the atomic clusters can significantly reduce the number of such atoms, but the need for them can not be completely removed. The potential for extrinsic vacancy formation in these regions is particularly relevant in the case of the metastable SI quasicrystals. Owing to the nature of the non-equilibrium processing (e.g. rapid solidification from the melt), vacancies (and voids) are expected to be quenched into the structure. The atomic clusters can possess an energetically favoured geometry within an undercooled liquid. Rapid solidification from the melt can therefore quench in these local atomic clusters, leaving the residual material to randomly occupy the interstitial regions. This is the basis of the icosahedral glass model which is now generally favoured for the metastable SI quasicrystals.

It is not clear, however, whether or not low temperature (i.e. below the crystallization temperature) annealing will prove effective at removing these defects (as is the case in conventional crystals). The lack of an underlying periodic structure may severely restrict the process of atomic diffusion.

Dislocations have now been successfully imaged via electron microscopy in quasicrystals [76,77,78,79,80,81,82] and a formal theoretical description has been established [71,83,84,85]. Within the hyperspace, dislocations can be defined in the conventional sense owing to the periodic arrangement of the atomic surfaces. However, subsequent projection results in Burgers vectors with non-zero components in $\mathbf{R}_{perp}$ and hence, an associated phason strain field (in addition to the usual phonon strain field). Restated, since quasicrystals lack well defined atomic planes, there are no easy glide planes and movement of dislocations necessarily require atomic diffusion. Thus the mobility of dislocations in quasicrystals is significantly reduced compared to their crystalline counterparts. It is for this reason that quasicrystals are extremely brittle [86].

3 Experimental details and data analysis

3.1 Introduction

The contents of this chapter are dedicated to a description of the positron annihilation techniques that are employed in this thesis work. Section 3.2 is devoted to a description of the positron source preparation procedures. Sections 3.3 and 3.4 detail the Doppler broadening and positron lifetime techniques, respectively. These techniques have been routinely employed for over twenty years and an extensive review of the general experimental considerations has previously been given by MacKenzie [87]. These details will generally not be reproduced here. However, a major part of this thesis work involved implementation of these techniques and specific details of this will be provided. In particular, an *in situ* Doppler broadening technique has been developed which utilizes the SLOWPOKE-2 thermal neutron flux for the production of a ^{64}Cu positron source. Both of these latter sections include not only a description of the instrumentation and experimental procedure, but also a performance evaluation of the technique. This is accomplished by comparing the experimental results on standard samples to those which have appeared in the literature. A description of the software which needed to be developed for the data collection and analysis is also given.

3.2 Positron source preparation

Two different positron sources have been employed. The first is an *external* source utilizing the positron emitting isotope, ^{22}Na, while the second is an *internal* source in which the isotope, ^{64}Cu, is produced *in situ* by neutron irradiation of a Cu containing sample. The decay schemes for ^{22}Na and ^{64}Cu are illustrated in appendix A and their relevant properties are listed in Table 3.1. A detailed account of the relative attributes

Isotope	$t_{1/2}$	N_{decay} [%]	ε_{max} [MeV]	ε_{γ} [MeV]	$\gamma_{positron}$ [%]		Prod.	$N.A.$ [%]
					Fiducial	Other		
^{22}Na	2.6y	90	0.545	1.275	100	11	^{19}F(α,n)	100
							^{24}Mg(d,α)	78.99
^{64}Cu	12.7h	19	0.573	-	0	2.5	^{63}Cu(n,γ)	69.2

Table 3.1: Properties of the positron sources. $t_{1/2}$ and N_{decay} are the isotope half-life and positrons per decay, respectively. ε_{max} and ε_{γ} correspond to the maximum energy of the emitted positron and the energy of the fiducial γ-ray, respectively. $\gamma_{positron}$ is the number of γ-rays per positron. The production reaction and natural abundance ($N.A.$) of the parent isotope are also included.

of these (and other) isotopes was given by MacKenzie [87] and will not be repeated here except for the following key points:

1. The rather short half-life for ^{64}Cu all but eliminates the option of purchasing the isotope from outside the institute. Instead, its use is restricted to those researchers in close proximity to a source of thermal neutrons. A SLOWPOKE-2 reactor [88] (details of the reactor architecture and flux characteristics are given in appendix B) is situated on the Dalhousie University campus thus affording us a rather unique opportunity to perform ^{64}Cu positron annihilation experiments.

2. Positron lifetime measurements require the emission of a fiducial γ-ray which flags the birth of the positron. The decay scheme for ^{22}Na (see Figure A.1 and Table 3.1) results in the emission of a 1.27 MeV γ-ray (with an intermediate state half-life of 3.7 psec) well within the spectrometer time resolution of the positron birth. Thus ^{22}Na is a suitable positron emitter for performing positron lifetime experiments. Unfortunately, the decay scheme of ^{64}Cu (see Figure A.2 and Table 3.1) does not result in a fiducial γ-ray precluding its use in positron lifetime experiments.

The most common external source preparation techniques involve deposition of the active solution (e.g. ^{22}NaCl(aq) + HCl(aq)) directly onto the surface of the sample or onto a thin backing material which is then covered with a second sheet of the same material. To facilitate the use of a single external source for all the measurements, the latter approach was adopted for the experiments reported in this thesis. In either case, the source is sandwiched between two sections of the sample with sufficient thickness (typically a few mm depending upon the sample material) to prevent annihilation of a measurable fraction of the positrons outside the sample, but thin enough to allow γ-ray emission.

The ^{22}Na source was prepared by depositing the solution, one drop at a time onto a 0.011 mm thick x 1.5 cm x 3 cm piece of the polyimide kapton using a small syringe. The center of the deposition was one quarter of the distance along the long symmetry axis of the kapton piece. The moisture was allowed to evaporate at room temperature between each application. The process was stopped after the deposition of a few μCi. The deposited salt formed a white homogeneous "stain" with a diameter of about 1 mm. The unactive half of the kapton piece was then folded over onto the active side and the three open edges sealed with super glue. To add rigidity to the source, it was fitted with a 0.5 mm thick square plastic frame (outer side length of 1.5 cm and an inner side length of 1 cm).

Kapton is the preferred backing material relative to the traditional metal foils for the following reasons:

1. The active salt is deposited uniformly over a disk shaped region. By comparison, deposition onto metal surfaces, tends to concentrate the activity into an annular ring-shaped region. This increase in the effective thickness of the source increases the proportion of positrons which annihilate within the salt.

2. Kapton possesses comparatively good mechanical properties and can be obtained in very thin sheets.

3. Positron annihilations within kapton do not indicate the formation of positronium (unlike in the case of mylar). As a result, only a single lifetime of 385 psec is observed which makes subtraction of the source contribution to the positron lifetime spectra relatively simple [87]. Metal foils tend to react with the weak acid solution resulting in additional source components. Furthermore, handling of the foils introduces defects which further complicate the source contribution to the annihilation spectra.

In addition to these attributes, kapton forms a very good vapour barrier rendering the source insensitive to changes in the humidity of the laboratory.

These points notwithstanding, the use of external sources possess a inherent disadvantage relative to the internal source. The thermal properties (atomic diffusion, reactivity, etc.) of the external source (particularly that of the backing material) severely restrict the range of temperatures which can be reliably and safely scanned. Even at low temperature, structural changes within the source material can occur leading to a complex dependence upon temperature [89].

The *in situ* ^{64}Cu sources were prepared by first sealing the Cu-containing samples in quartz tubes under a half atm of Ar and then subjecting them to the thermal neutron flux, Φ. The expected activity, $\mathcal{A}$, resulting from neutron capture can be calculated using the expression,

$$\mathcal{A}(t)[Ci] = (2.7 \times 10^{-11})(\sigma_c \Phi (m/A))(1 - e^{-\lambda t}). \tag{3.1}$$

$$\left[\begin{array}{ll} \sigma_c & = \textit{thermal neutron cross section } [barns] \\ \Phi & = \textit{thermal neutron flux } [n/barn/sec] \\ m & = \textit{mass of parent isotope } [g] \\ A & = \textit{atomic mass of parent isotope } [g/atom] \\ \lambda & = \textit{decay rate of radioactive isotope } [/sec] \end{array}\right.$$

Further details can be found in appendix C.

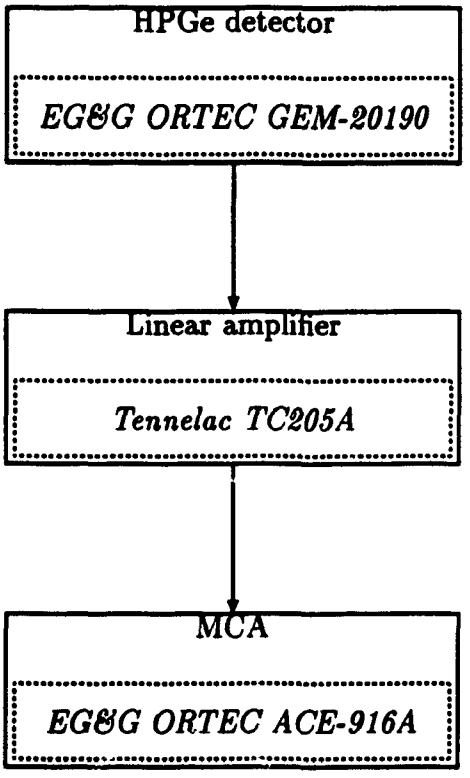

Figure 3.1: Schematic of the Doppler broadening spectrometer.

3.3 Doppler broadening techniques

3.3.1 General experimental details

Figure 3.1 gives a schematic representation of the Doppler broadening (DB) spectrometer. The EG&G ORTEC GEM-20190 HPGe detector has a 22% efficiency @1.33 MeV. The multichannel analyzer (MCA) consists of an EG&G ORTEC ACE-916A 8k successive approximation analog-to-digital converter (ADC) card mounted in a host PC. Data acquisition is controlled using the MCA emulation software package, MAESTRO II.

The intent of the DB technique is to measure the energy distribution from the 2-γ annihilation process, $\mathcal{P}^{2\gamma}(\varepsilon)$. Such a distribution is roughly centered on the rest

energy, E_o (=511keV), of the electron. However, the center of mass velocity, v, of the electron/positron pair at the moment of annihilation results in a shift in the γ-ray energies within the limits,

$$\varepsilon = \pm m_o c v \tag{3.2}$$

where m_o and c are the rest mass of the electron and the speed of light, respectively.

The measured discrete spectrum, $C_i^{2\gamma}$, is a convolution of the energy spectrum of the γ-rays (i.e. $\mathcal{P}^{2\gamma}(\varepsilon)$)[1] with the energy resolution, $\mathcal{R}(\varepsilon)$, of the spectrometer,

$$C_i^{2\gamma} = \frac{1}{\Delta\varepsilon}\int_{\varepsilon_i-\Delta\varepsilon/2}^{\varepsilon_i+\Delta\varepsilon/2}\left[\int_{-\infty}^{+\infty}\mathcal{R}(\varepsilon'-\varepsilon)\mathcal{P}^{2\gamma}(\varepsilon')d\varepsilon'\right]d\varepsilon + \mathcal{B}_i + \mathcal{F}_i, \tag{3.3}$$

where ε_i, $\Delta\varepsilon$, $\mathcal{B}_i$ and $\mathcal{F}_i$ are the energy corresponding to channel i, the energy interval per channel, the background component of the channel count and the noise component of the channel count (Poisson distributed), respectively. Figure 3.2 shows a typical DB spectrum along with the measured resolution function.

In the case of a simple metal [2], $\mathcal{P}^{2\gamma}(\varepsilon)$ is well approximated by a superposition of two distributions: (a) a gaussian representing the collective contribution from core electron annihilations; and (b) a parabola representing annihilations with (free) conduction electrons. That is, $\mathcal{P}^{2\gamma}(\varepsilon)$ is fit to the model

$$\mathcal{P}^{2\gamma}(\varepsilon) = \begin{cases} \frac{A}{\sqrt{2\pi}\sigma_g}e^{-(\varepsilon-\varepsilon_g^o)^2/(2\sigma_g^2)} + B - C(\varepsilon-\varepsilon_p^o)^2 & ;|\varepsilon-\varepsilon_p^o| \le \sqrt{\frac{B}{C}} = \sqrt{\frac{\varepsilon_F E_o}{2}} \\ \frac{A}{\sqrt{2\pi}\sigma_g}e^{-(\varepsilon-\varepsilon_g^o)^2/(2\sigma_g^2)} & ;\text{otherwise} \end{cases} \tag{3.4}$$

where A, B, C, σ_g, ε_g^o and ε_p^o are adjustable parameters. ε_F is the Fermi energy of the conduction electrons.

Smearing of the $\mathcal{P}^{2\gamma}(\varepsilon)$ features by $\mathcal{R}(\varepsilon)$ can not be ignored since the full width at half maximum (FWHM) of $\mathcal{R}(\varepsilon)$ is typically no less than about 50% that for $C^{2\gamma}(\varepsilon)$ [3].

[1]Note that $\mathcal{P}^{2\gamma}(\varepsilon)$ includes any annihilations from within the source as well as from within the sample.

[2]Modification of the model is required upon introduction of, for example, band-structure effects (non-spherical Fermi surface).

[3]In principle, the angular correlation (ACAR) technique measures the equivalent physics, i.e. the momentum distribution of the electron/positron pair. Since the geometry in such an experiment can

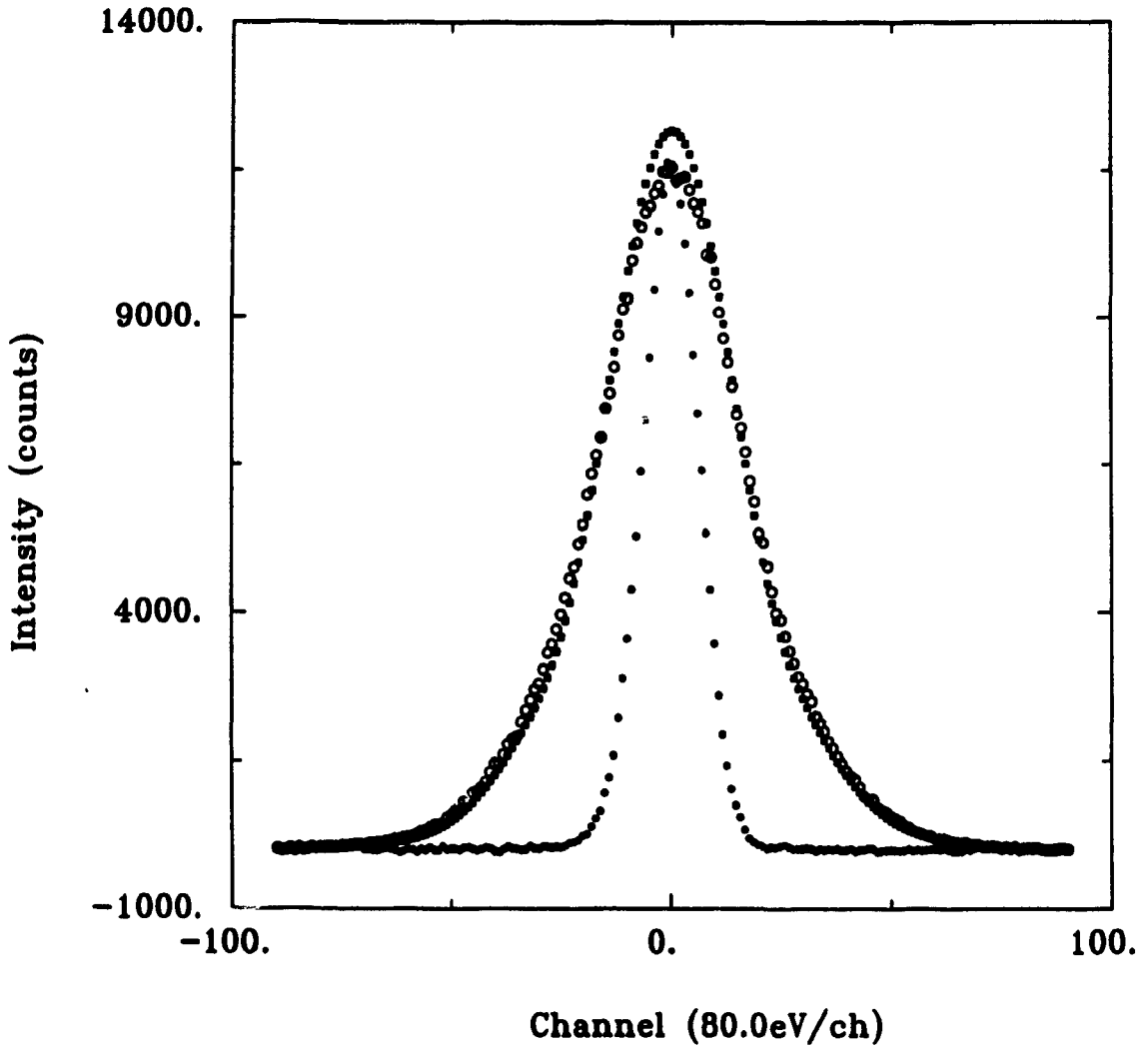

Figure 3.2: Typical DB spectrum (o) for Cu measured at room temperature using the *in situ* technique (see text). Also included in the figure is the simultaneously measured resolution spectrum (•) using a ^{103}Ru source and the deconvoluted spectrum (■) obtained by the direct space technique (see text).

A ^{103}Ru calibration source is used to monitor $\mathcal{R}(\varepsilon)$ during the data collection. The nuclear decay scheme for ^{103}Ru, which is illustrated in appendix A, reveals why it is well suited for this purpose.

1. The principal γ-ray energy of 497.08keV resulting from the decay scheme is quite close to the annihilation energy of 511keV but without significant overlap. Thus simultaneous measurement of the two spectra is possible.

2. The nuclear states responsible for the principal γ-ray are sufficiently long-lived to ensure that the natural width of the energy distribution will be practically zero (i.e. $\ll$1eV).

3. The half-life of 39.4 days is sufficiently long for ease of operation.

The ^{103}Ru source was prepared by embedding a few mg of elemental Ru powder in epoxy followed by irradiation at SLOWPOKE-2 [4].

Taking the ^{103}Ru spectrum to be indicative of $\mathcal{R}(\varepsilon)$ for the spectrometer, typical parameter settings of:

$$\left[\begin{array}{ll} HV & = +2700V \\ Gain & = \times 500(fine: 7.58) \\ Shaping & = 3\ \mu sec \\ Channel\ calibration & = 80eV/ch \\ Run\ time & = 1\ hour \\ Source & = ^{103}\ Ru \\ Count\ rate & = 2.4\ kilocounts/sec \end{array}\right.$$

result in a FWHM @497keV of 1.27(8)keV for the DB spectrometer.

$\mathcal{R}(\varepsilon)$ is most sensitive to two factors:

---

be arranged to make $\mathcal{R}$(p) arbitrarily narrow, one would expect that the ACAR technique would be favoured. However, the ACAR technique is a coincidence experiment and the data through-put is several orders of magnitude lower than that for the DB technique. The higher statistical precision for the DB data compensates for the poorer resolution.

[4] In addition to ^{103}Ru, neutron capture results in the production of ^{97}Ru ($t_{1/2}$=2.88days) and ^{105}Ru ($t_{1/2}$=4.44hours). To ensure that the calibration source flux is not changing appreciably over the course of the experiments, the as-prepared source is allowed to cool for approximately one week before use.

1. The effective gain of the amplifier and ADC, even when operating within their specifications, have an appreciable sensitivity to ambient temperature. For typical operation parameters, each are expected to contribute a spectrum shift of ~1 ch/°C (~80 eV/°C). A combined 2.1ch/°C anti-correlation is observed for the 662keV photo-peak position of ^{137}Cs as the ambient temperature is varied.

2. Pulse pile-up distortion of the photo-peak becomes increasingly significant as the count rate increases. Figure 3.3 illustrates how the full width at various maxima (FWxM) and the peak position of the 497keV photo-peak of ^{103}Ru change as the incident flux on the detector is increased.

Digital stabilization of the spectrum is the preferred method of dealing with the temperature instability. This option was not available during the course of this thesis work, so precautions needed to be taken to ensure a minimal variance in ambient temperature during the data collection process. The individual collection times were therefore limited to no more than 30 min, during which a change in the ambient temperature of no more than 0.5°C/hr resulted in tolerable distortions to $\mathcal{R}(\varepsilon)$.

As a compromise between the desire for maximizing the data through-put and minimizing the effects from pulse pile-up distortion of $\mathcal{R}(\varepsilon)$, the experiments were run with a total incident flux on the detector which resulted in a DT=~20%.

3.3.2 *In situ* technique

In addition to the above considerations, a few specific concerns regarding the *in situ* technique are now addressed.

Assuming a cylindrical detector with a radius of, r, and a source at a distance, d, along the detector axis, the rate of change, $\Omega = dd/dt$, required to maintain a constant incident flux is given by,

$$\Omega = -\left(\frac{ln2}{t_{1/2}}\right)\left[1 - \frac{d}{\sqrt{r^2+d^2}}\right]\left[\frac{(r^2+d^2)^{3/2}}{r^2}\right] \tag{3.5}$$

where $t_{1/2}$ is the source half-life. The relatively short half-life of the ^{64}Cu isotope necessitates the periodic adjustment of d. Since Ω is not a simple function of time,

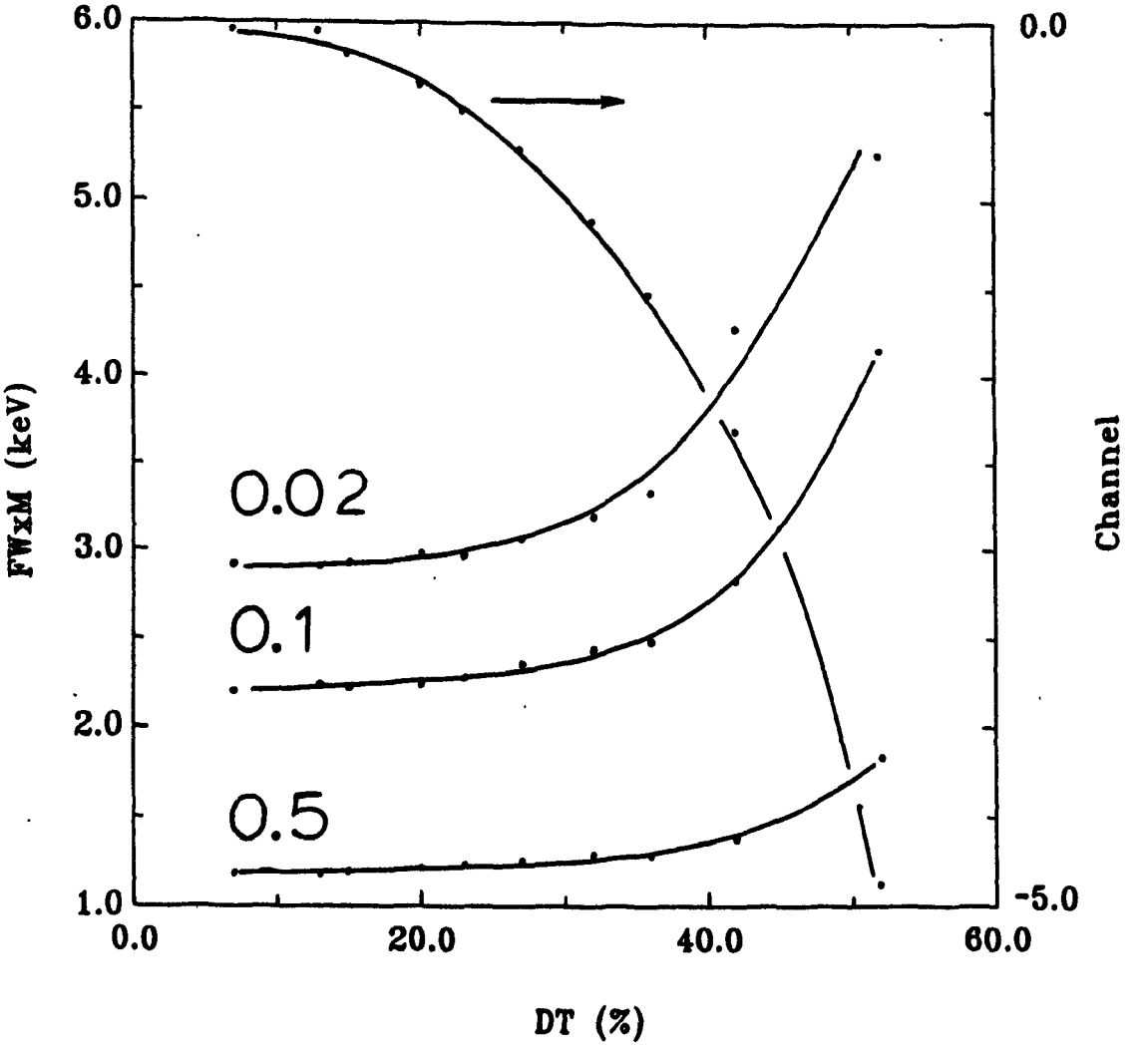

Figure 3.3: Full width at various maxima (FWxM; x=0.02, 0.1 and 0.5) and peak position of the 497 keV ^{103}Ru photo-peak (relative to that at DT=0%) as a function of ADC dead time, DT. The ^{103}Ru source flux corresponded to DT=7% and was held constant whereas the additional flux was produced with a ^{64}Cu source. Each spectrum was acquired for a live time equal to 5 min.

continuous adjustment of d would be tedious. However, the choice of DT=20% is sufficiently low to allow for measurement run times of 10 min at a constant d without appreciable distortion to $\mathcal{R}(\epsilon)$. Nevertheless, during the course of a series of measurements, this distance requires periodic adjustment.

A small vertical tube furnace (see Figure 3.4) was used to perform the temperature scans on the samples. This furnace has been used to heat samples up to 1000°C. Its light-weight construction and compactness meant that it could be suspended off the side of a jiffy-jack to facilitate vertical translation. In this way, a DT=20% can be maintained for up to 48 hours for a typical starting activity of 300μCi. Beyond this, the design specifications were not demanding.

1. The goal of the temperature scans was to identify the coarse changes in the sample defect behavior over a wide temperature range (above room temperature). It was anticipated that a minimum temperature step of 25°C would be sufficient. A vertical temperature gradient of ~10°C/cm is observed near the center of the furnace at 800°C. Thus a temperature gradient of no more than 5°C can be achieved by restricting the vertical dimension of the sample to less than 0.5cm. The heater current was adjusted manually resulting in a temperature stability of ±1°C over the data collection interval.

2. There was no need for an inert gas atmosphere enclosure since the samples will have been previously sealed in quartz.

3. The rather high energy of the annihilation γ-rays allow for conventional construction materials although approximately 17% attenuation of the photo-peak intensity was observed for a ^{64}Cu source inside the furnace relative to outside.

3.3.3 Data analysis

In this section, specific details regarding analysis of the DB annihilation spectra are presented.

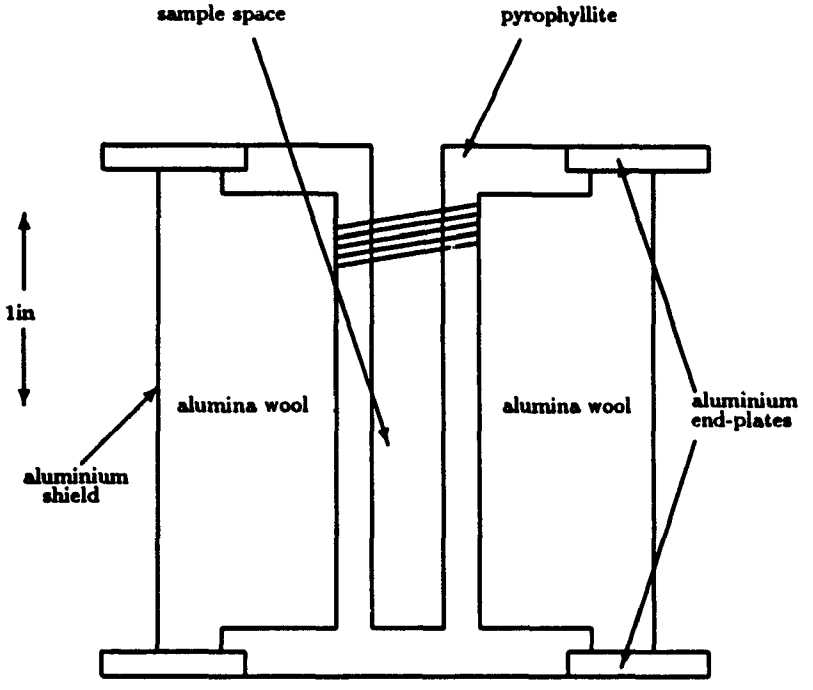

Figure 3.4: Schematic of the furnace. Chromel-alumel thermocouples are inserted through the top along with the sample sealed in quartz. The heating wire is Kanthal A1 with a coil density of 20 turns/in.

The high efficiency of the HPGe detector ensures that low energy tailing (resulting from incomplete charge collection) of the photo-peaks is not a significant problem. A linear background is therefore fit and subsequently subtracted from each peak (i.e. the ^{103}Ru resolution peak and the annihilation peak). In each case, a five channel (0.4 keV) region is selected from either side of the peak centroid. The average counts in each region is then used as endpoint values for the linear background. The regions are centered at $\pm$6.2 keV and $\pm$5.4 keV for the annihilation and ^{103}Ru peaks, respectively.

The peak centroids are determined by fitting the central FWHM channels to a gaussian using a Levenberg-Marquardt [90] nonlinear least-squares routine. The spectra are then shifted by spline interpolation such that the central channel corresponded to the fitted gaussian centroid to within the nearest 100th of a channel.

After the background subtraction and peak-centroid shift, the annihilation spectrum is characterized using the lineshape parameters [91,92,93]:

$$S = (\sum_{i=-n}^{n} C_i^{2\gamma})/(\sum_{i=-N/2}^{N/2} C_i^{2\gamma}), \tag{3.6}$$

$$L = (\sum_{i=-n}^{n} C_i^{2\gamma})/(\sum_{i=-m}^{-n} C_i^{2\gamma} + \sum_{i=n}^{m} C_i^{2\gamma}); \quad m > n, \tag{3.7}$$

and

$$W = (\sum_{i=-n}^{-m} C_i^{2\gamma} + \sum_{i=n}^{m} C_i^{2\gamma})/(\sum_{i=-N/2}^{N/2} C_i^{2\gamma}); \quad m > n, \tag{3.8}$$

where N is the number of channels in the spectrum array, $C_i^{2\gamma}$ is the number of counts corresponding to channel (energy) i, i=0 corresponds to the peak centroid and n and m are chosen to encompass the immediate region around the centroid and the wing areas, respectively.

Uncertainties in the lineshape parameter values correspond to 50% confidence intervals based upon a statistical analysis of 10 measured spectra. Typical uncertainties of 0.2-0.4% are found for spectra containing an integrated intensity of $5\text{x}10^5$ counts.

For the present purpose, i.e. flagging changes in sample defect behavior, the choice of parameter is not critical. The S parameter is by far the most commonly used, but its sensitivity to changes in the defect structure depends critically upon the choice of n. In situations where the variance in defect behavior is expected to be quite complex, the L parameter is generally quite sensitive to all changes and n and m can be fixed to facilitate comparison of different samples.

Figure 3.5 shows S as a function of temperature from *in situ* measurements on elemental Cu. The sigmoidal trend to the data is characteristic of a two-state trapping model (see e.g. [94]) due to thermally generated monovacancies in which the positron-trapping rate is given by

$$\kappa_{1v}(T) = \lambda_b \left[\frac{F(T) - F_b(T)}{F_{1v}(T) - F(T)}\right] = \mu_{1v} e^{s_{1v}/k_B} e^{-H_{1v}/k_B T}. \tag{3.9}$$

Researcher(s) (year)	technique	H_{1v} [eV]	Ref.
Fukushima *et. al.* (76)	ACAR	1.21(2)	[96]
Rice-Evans *et. al.* (76)	DB	1.26(7)	[97]
Berger *et. al.* (79)	resistivity	1.30(5)	[98]
Fluss *et. al.* (80)	DB	1.31(5)	[99]
Lawther (93)	DB	1.21(2)	⋆

Table 3.2: Comparison of the determined value for the enthalpy of vacancy formation, H_{1v}, in Cu with those previously published in the literature. ⋆ denotes this work.

F_b and F_{1v} correspond to one of the lineshape parameters (denoted by F) resulting from annihilations exclusively from the delocalized and localized (i.e. within a monovacancy) positron states, respectively. μ_{1v} is the specific positron-trapping rate per unit defect concentration, λ_b is the bulk positron annihilation rate (=9.09x10^{-3}/psec [95] for Cu), k_B is the Boltzmann constant and s_{1v} and H_{1v} are the entropy and enthalpy of vacancy formation, respectively.

A least-squares fit to this model is also shown in Figure 3.5. The resulting value for H_{1v} (=1.21(2)eV) compares favourably with those previously published using DB, angular correlation of annihilation radiation (ACAR) and resistivity techniques (see Table 3.2).

A detailed analysis of the electron energy distribution requires deconvolution of $\mathcal{R}_i$ from $C_i^{2\gamma}$. Two approaches have been explored and are described in turn below.

Deconvolution in direct space [100,101]. An initial guess $\mathcal{P}_i^{(0)}$ (usually the convoluted annihilation spectrum, $C_i^{2\gamma}$) is convoluted with $\mathcal{R}_i$,

$$C_i^{(0)} = \sum_{j=-N/2}^{N/2} \mathcal{R}_{j-i}\mathcal{P}_j^{(0)} \tag{3.10}$$

and

$$\chi^2 = \sum_{i=1}(C_i^{(0)} - C_i^{2\gamma})^2/C_i^{2\gamma} \tag{3.11}$$

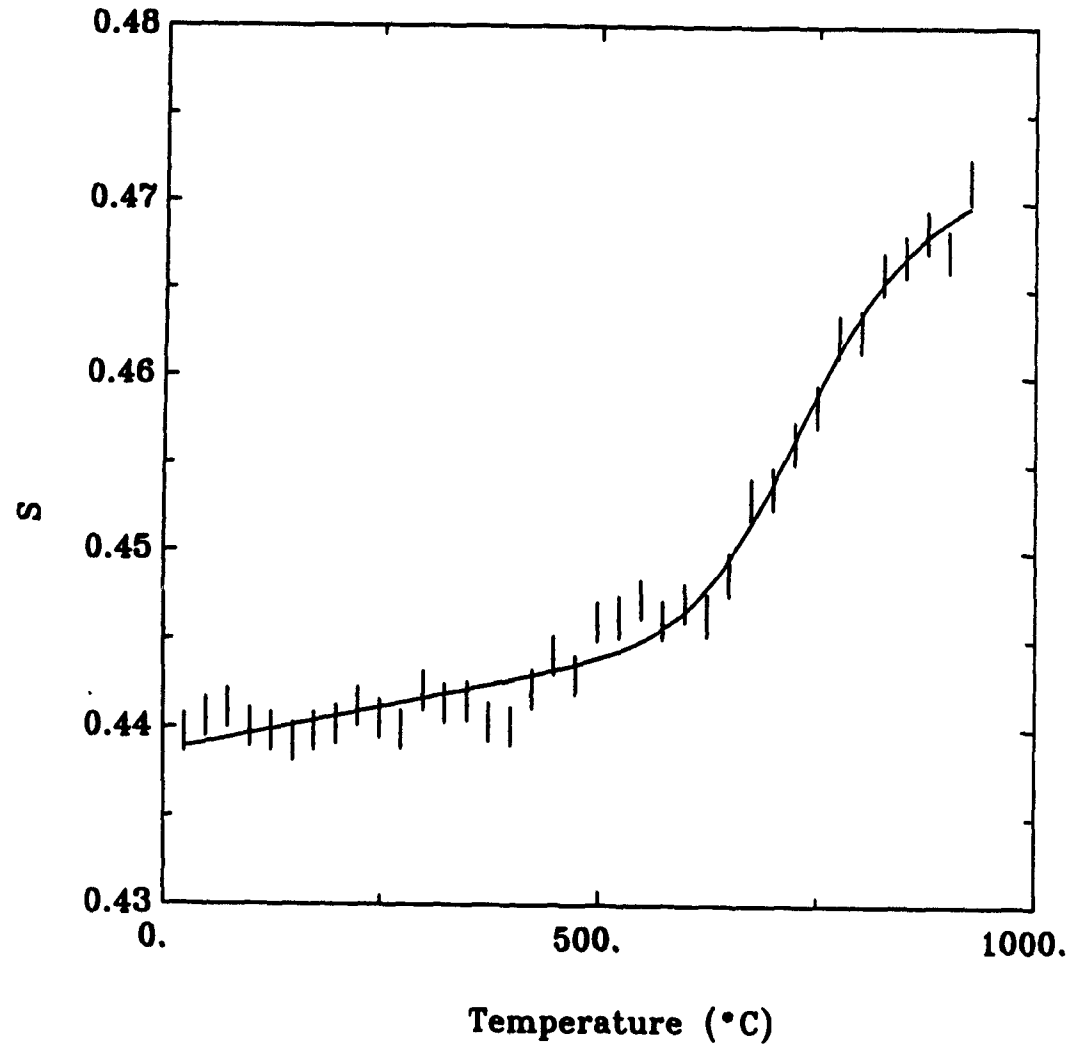

Figure 3.5: S as a function of temperature from *in situ* DB measurements on elemental Cu. Also shown in the figure is a fit to a two-state trapping model as described in the text.

calculated. $\mathcal{P}_i^{(0)}$ is then modified by a multiplication factor [100],

$$\mathcal{M}_i = (\sum_{j=-l}^{l} \mathcal{C}_{i+j}^{(0)})/(\sum_{j=-l}^{l} \mathcal{C}_{i+j}^{2\gamma}) \tag{3.12}$$

and the process repeated until χ^2 is minimized.

An unfortunate side-effect from the use of $\mathcal{M}_i$ is the introduction of a limit to the curvature of $\mathcal{C}_i^{(0)}$. The consequences of this are: (a) an over-estimate of the first moment of the deconvoluted annihilation peak; and (b) the generation of artifact oscillations radiating out from sharp Fermi surface features. The latter can be significantly reduced by repeating the above deconvolution procedure with successively larger values for l (typically in the range l=3 to l=7) but only at the expense of the former.

Nevertheless, the zeroth moment of the deconvoluted spectrum is not significantly corrupted. Subsequent least-squares fitting to a model distribution can result in reliable estimates of the relative intensities of components (even though an over-estimate for the Fermi energy may result). Figure 3.6 gives the (relative) parabolic intensity, I_p ($=\frac{4}{3}B\sqrt{B/C}$), as a function of temperature from fits of the deconvoluted Cu spectra (i.e. Figure 3.2) to expression 3.4. Note that I_p is roughly constant at ~25% from room temperature up to ~500°C, above which it rises monotonically to ~31% at 925°C. This agrees well with the results reported by Rice-Evans *et. al.* [97] in which an increase from ~23% to ~33% was observed. This increase is a reflection of the increased proportion of the positrons annihilating from trap sites (i.e. monovacancies).

Deconvolution in Fourier space [102,103,104,105]. The Fourier transform of equation 3.3 (ignoring the linear background) is

$$c_z = r_z p_z + f_z, \tag{3.13}$$

where c_z, r_z, p_z and f_z are the N_{FT} discrete Fourier components of $\mathcal{C}_i^{2\gamma}$, $\mathcal{R}_i$, $\mathcal{P}_i^{2\gamma}$ and $\mathcal{F}_i$, respectively. The angular frequency, ω, related to the Fourier coefficient, z, is

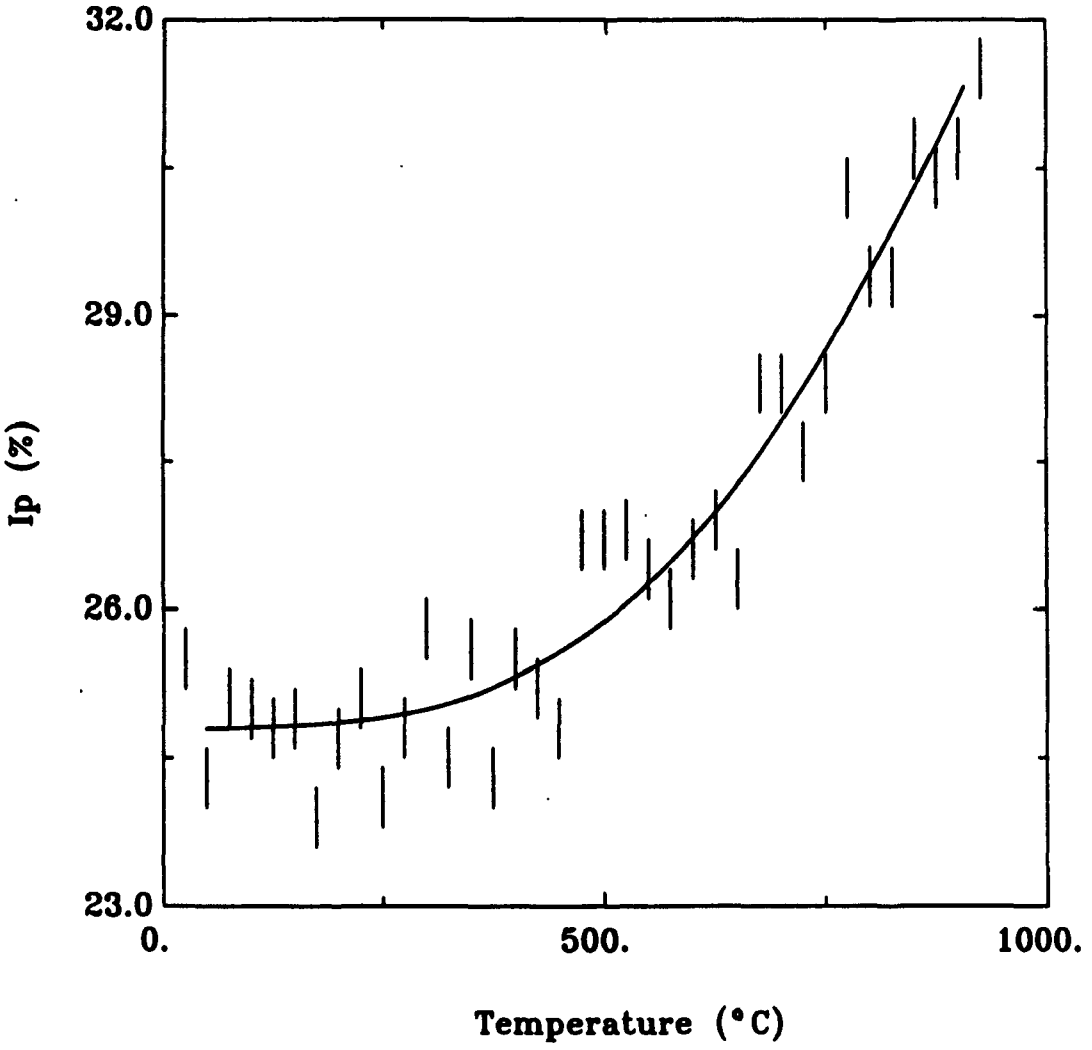

Figure 3.6: I_p as a function of temperature from a fit of expression 3.4 to direct space deconvoluted Cu DB spectra. The curve is a visual guide only.

given by,

$$\omega = 2\pi z/N_{FT}. \tag{3.14}$$

Thus the deconvolution involves a simple component-by-component division,

$$p_z^{decon} = c_z/r_z = p_z + f_z/r_z. \tag{3.15}$$

Clearly $p_z^{decon} \neq p_z$ due to the noise contribution, f_z/r_z. In fact, the finite widths of $C_i^{2\gamma}$ and $\mathcal{R}_i$ and the randomness of $\mathcal{F}_i$, ensure that f_z/r_z will dominate p_z^{decon} at large z [5]. Nevertheless, it has been found [106] that reliable information can be extracted from a least-squares fit of the low z region of the Fourier spectrum to a model function. For example, in the simple metal model (i.e. equation 3.4), the Fourier components are fit to the function,

$$p(\omega) = \left\{ A' e^{-\omega^2\sigma_p^2/4} + \frac{B'}{\omega^2\sigma_p^2}\left[\frac{\sin\omega\sigma_p}{\omega\sigma_p} - \cos\omega\sigma_p\right]\right\} e^{(\omega/2R_o)^2} \tag{3.16}$$

where A', B', σ_p and R_o are parameters to be fit. The first term is the Fourier transform of a gaussian (core contribution) and the second term is the Fourier transform of a parabola (free electron contribution). The exponential damping factor has been introduced to account for possible localization of the positron to within a spatial extent of R_o [106].

In expression 3.16, the zeros of the second term,

$$\sigma_p\omega^{(i)} = 4.493, 7.725, 10.904..., \tag{3.17}$$

can be related to the Fermi energy by

$$\varepsilon_F^{(i)} = \left(\frac{2}{E_o}\right)\left[\sigma_p/\omega^{(i)}\right]^2. \tag{3.18}$$

Determination of both R_o [106] and ε_F (see e.g. [107]) have been successfully demonstrated from ACAR spectra. However, the inability of the DB technique to extract Fourier components beyond the first zero in expression 3.17 prevents a duplication of these successes beyond the most favourable conditions.

[5] The deconvolution actually amplifies the noise, necessitating the application of a low-pass filter to the Fourier space data. Unfortunately, this procedure tends to generate unphysical oscillations in the resulting inverse Fourier transformed deconvoluted spectrum.

3.4 Positron lifetime technique

3.4.1 Experimental details

Figure 3.7 gives a schematic representation of the positron lifetime spectrometer. It is a fast timing coincidence system using Harshaw $1\frac{7}{8}$ in dia. x $1\frac{1}{2}$ in CsF scintillation crystals mounted on Hamamatsu R2083 photomultiplier tube (PMT) assemblies. A voltage of -2700 V is supplied to the PMT's with an HP 6516A PS. ORTEC 583 constant fraction differential discriminators (CFDD) perform the energy selection as well as furnishing the fast negative output signals for the TENNELAC TC861A time-to-analog converter (TAC). The delay on the STOP side of the TAC is implemented using a RG-58/U co-axial cable (1.542 nsec/ft) 18.2 ft in length (28.1 nsec). The ORTEC 414 fast coincidence window is set at 50 nsec. The data are collected on a ND62 MCA. A detector-source-detector collinear geometry is employed with a 2 mm lead shields over the crystals to eliminate detection of multiply scattered γ-rays.

The spectrometer performance was characterized by measurement of the prompt coincidence peak of ^{60}Co using the energy window settings appropriate for the ^{22}Na source. For an approximate source strength of 5 μCi and a coincidence rate of 70 counts/sec, the peak-to-background ratio is 6600:1 and the FWHM of the prompt coincidence peak is 400 psec. The peak is well fit to one gaussian (although two additional low intensity gaussians are needed to accurately fit the positive and negative time tails) and this has proven adequate for the subsequent spectral analysis. The time calibration (=24.9(1) psec/ch) was determined by interchanging the delay cable with one 25.0 ft long and observing the shift in the prompt coincidence peak of ^{60}Co.

The operating conditions for the collection of each positron lifetime spectrum were as follows. The experimental run time was 5 hr with a spectrum intensity of $1x10^7$ counts. The individual count rates were 7000 counts/sec (START) and 10000 counts/sec (STOP) and the coincidence rate was 570 counts/sec. The peak-to-background ratio was 12500:1. A typical lifetime spectrum is given in Figure 3.8.

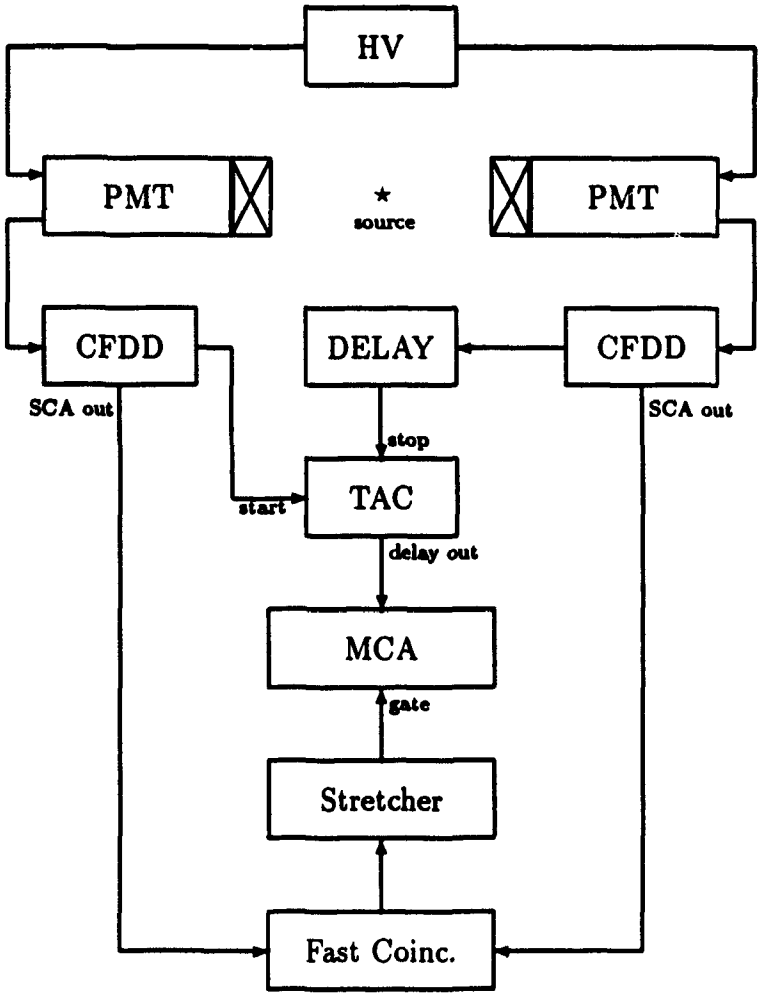

Figure 3.7: Schematic of the positron lifetime spectrometer.

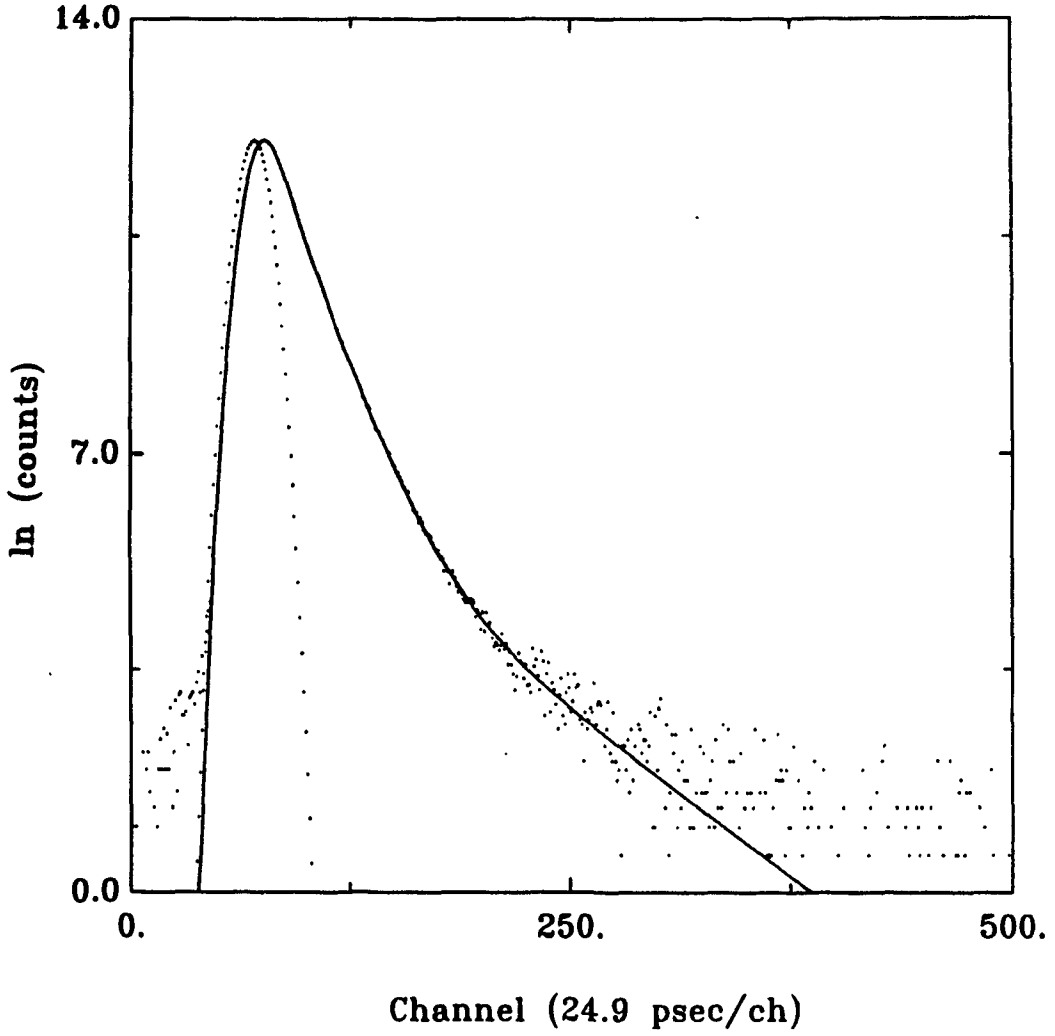

Figure 3.8: Room temperature positron lifetime spectrum for Bi and the result from a fit (see text) to a gaussian resolution function convoluted with three exponential components. Also included in the figure is the fitted resolution function centered on zero time, t_o.

3.4.2 Data analysis

Analysis of the positron lifetime spectra is performed with a program which is functionally equivalent to the commercially available software, POSITRONFIT [108,109, 110]. The spectrum, $C^{2\gamma}(t)$, is assumed to be a superposition of discrete lifetime components of the form,

$$I_j(t) = \begin{cases} I_{oj}exp(-\lambda_j t) & ; \text{if } t \geq 0 \\ 0 & ; \text{otherwise} \end{cases} \tag{3.19}$$

convoluted with a time-resolution function, $\mathcal{R}(t)$. τ_j is the jth component lifetime ($=1/\lambda_j$, where λ_j is the annihilation rate) and I_{oj}/λ_j is its relative intensity.

In the case of a gaussian resolution function,

$$\mathcal{R}(t) = \left(\frac{1}{\sqrt{\pi}\sigma_g}\right) exp[-(t-t_o)^2/\sigma_g^2], \tag{3.20}$$

the discrete spectrum (averaged over a channel width) is,

$$C_i^{2\gamma} = \sum_j \left(\frac{I_{oj}}{2\lambda_j}\right)\left[Y_{j,i} - Y_{j,i+1} - erf\left(\frac{t_i - t_o}{\sigma_g}\right) + erf\left(\frac{t_{i+1} - t_o}{\sigma_g}\right)\right] + \mathcal{B}_i + \mathcal{F}_i \tag{3.21}$$

and

$$Y_{j,i} = e^{[-\lambda_j(t_i - t_o) - \frac{1}{4}\lambda_j\sigma_g^2]}\left\{1 - erf[\frac{1}{2}\lambda_j\sigma_g - (t_i - t_o)/\sigma_g]\right\} \tag{3.22}$$

where $erf(t)$ is the error function, $\mathcal{B}_i$ is the channel background count and $\mathcal{F}_i$ is the Poisson distributed statistical noise contribution.

After subtraction of a linear background, the spectra are fit to expression 3.21 (the program is not restricted to a single gaussian) using a Levenberg-Marquardt [90] nonlinear least-squares routine. Since $\mathcal{R}(t)$ is quite sensitive to the operating conditions (count rate, energy distribution, etc.), σ_g is a parameter to be fit for each spectrum.

The uncertainties in the fitted parameters correspond to 50% confidence intervals based upon a Monte Carlo method using 10 generated spectra. The generated spectra are constructed by superimposing a gaussian distributed random noise [6] (i.e. a

[6] This is a good approximation to the Poisson distribution provided the channel count is greater than ~100.

Element	τ_b [psec]	σ_g [psec]	τ_1 [psec]	τ_2 [psec]	I_2 [%]	I_3 [%]	VOF
Zn	148 [111]	238(2)	160(2)	983(50)	2(5)	16(4)	1.3
Sn	201 [112]	234	200	1085	1	19	1.1
Bi	234 [112]	239	230	1212	2	21	1.3

Table 3.3: Results from fits of elemental sample positron lifetime spectra to a gaussian convoluted with three component lifetimes. τ_b corresponds to the bulk lifetime values which have been published in the literature. τ_1 and τ_2 correspond to the measured bulk lifetime for the element and the NaCl of the source, respectively. τ_3 was fixed at 385 psec corresponding to the bulk positron lifetime for kapton. VOF is the variance-of-fit obtained from the fitting procedure.

random generator produces a channel noise contribution which has a gaussian probability distribution with $\sigma_i = \sqrt{C_i}$) onto a model spectrum, C_i (constructed from the fitted parameters to the experimental spectrum).

Table 3.3 gives the results from a fit of the positron lifetime spectra for well-annealed elemental Zn, Sn and Bi to a gaussian convoluted with three components. The fit to the Bi sample is given in Figure 3.8. All parameters were free except for one component lifetime which was fixed at that for kapton (τ_3=385 psec). The measured bulk lifetimes (τ_1) are in good agreement with those which have been previously published although the result for Zn is approximately 10 psec too high. This is a reflection of the tendency for the resolution function parameter (i.e. σ_g) to be highly correlated with the shorter lifetimes.

4 Positron annihilation studies of quasicrystals

To date, there have been more than a dozen reported positron annihilation investigations of quasicrystals. A chronology of these can be found in Table 4.1 and a brief accounting of the results is given below.

Metastable quasicrystals: Much of the earlier work was performed on metastable quasicrystals (Al-Mn [114,119], Al-Mn-Si(Ru) [113,115,116,123,124,130], Al-Cu-V [132] and Al-Cu-Mg [119]) produced by rapid solidification from the melt. There is considerable variation in the results do to the uncertainties associated with the sample preparation procedures employed. However, an overall concensus can be reached regarding the important features of the data.

Positron lifetime and the DB measurements indicate that the as-quenched samples contain extrinsic vacancy defects (variable from monovacancies up to at least trivacancies depending upon the quenching conditions) in concentrations, c ($\sim$ few 10^{-6}), between those for closely related amorphous and crystalline phases. In the case of Al-Mn-Si [113],

$$c_{cryst} \simeq c_{quasi} \simeq 0.2 c_{amorph}. \tag{4.1}$$

Typically, 10-60 % of the positrons annihilate from such trap sites with a lifetime in the range of 250-300 psec.

A comparison of the positron lifetime spectra for the icosahedral $Al_{74}Mn_{20}Si_6$ and the closely related crystalline α-Al-Mn-Si was reported by Kanazawa *et.al.* [130]. The lifetime spectrum for α-Al-Mn-Si consists of a single component with a lifetime of $\sim$200 psec corresponding to saturation trapping of the positrons in the vacant center of the Mackay icosahedra (see Figure 2.3(a)). Conversely, the lifetime spectrum for the icosahedral phase possesses a bulk component of $\sim$170 psec (and a component

Researcher(s) (year)	Description	Ref.
Dunlap, Lawther and March (87)	DB(RT) on Al-Mn-Si	[113]
Sanyal *et. al.*(89)	DB(RT) on Al-Mn	[114]
Kizuka *et. al.*(89)	L(RT),DB(RT) on Al-Mn-Si	[115]
Chidanbaram *et. al.*(90)	L(RT),DB(RT) on Al-Mn-Si	[116]
Chidanbaram *et. al.*(90)	L(RT),DB(RT) on Al-Cu-Li	[117]
Ohata *et. al.*(90)	L(RT),DB(RT) on Al-Cu-Li	[118]
Kanazawa *et. al.*(90)	L(RT),DB(RT) on Al-Mn and Al-Cu-Mg	[119]
Lawther *et. al.*(90)	DB(RT) on Al-Cu-A (A=Fe,V)	[120]
Chidanbaram *et. al.*(90)	L(RT),DB(RT) on Al-Cu-Fe	[121]
Howell *et. al.*(92)	L(T≤RT),ACAR(T≤RT) on Al-Cu-Fe	[122]
Shi *et. al.*(92)	L(RT), DB(RT) on Al-Cu-Li	[123]
Kanazawa *et. al.*(92)	L(RT) on Al-Mn-Si(Ru) and Al-Cu-Li	[124]
Kristiakova *et. al.*(92)	L(RT) on Al-Cu-Fe	[125]
Nakao *et. al*(92)	L(RT),ACAR(RT) on Al-Ni-Co	[126]
Lawther and Dunlap (93)	DB(RT) on Al-Cu-Fe	[127],⋆
Lawther and Dunlap (93)	L(RT),DB(T) on Al-Cu-Fe	[128],⋆
Chidanbaram *et. al.*(93)	L(RT) on Al-Cu-Fe	[129]
Kanazawa *et. al.*(93)	L(RT) on Al-Mn-Si-Ru	[130]
Lawther and Dunlap (93)	L(RT),DB(T) on Al-Cu-Fe	[131],⋆

Table 4.1: Chronology of reported positron annihilation measurements on quasicrystals. L, DB and ACAR denote positron lifetime, Doppler broadening and angular correlation of annihilation radiation measurements, respectively. RT and T denote measurements at room temperature and as a function of temperature, respectively. (⋆) indicates work to be reported in this thesis.

corresponding to vacancies) indicating a reduction in the size of the vacant cluster centers. The substitution of Ru for both Si and Al further reduces the bulk component to ~145 psec. This is consistent with recent total-energy calculations [133] which indicate that occupation of the cluster centers is energetically favoured (although this result makes no distinction between the icosahedral phase and the α-phase).

Subsequent isochronal annealing of the samples [114,115,116,119] indicates that the smaller extrinsic defects are mobile above 200°C. For large concentrations of these quenched-in defects, accretion can occur. Complete annihilation of these defects has not been observed to occur prior to crystallization. This behavior is illustrated in Figures 4.1 and 4.2 in which selected published results have been reproduced.

Stable quasicrystals: Thermodynamically stable SI Al-Cu-Li [117,118,123,124] and FCI Al-Cu-Fe [120,121,122,125,129] have been studied both in the as-prepared state and as a function of isochronal anneal temperature.

For Al-Cu-Li, decomposition of the positron lifetime spectra indicates that at least 80% of the positrons annihilate from a vacancy-like trap site (τ ~220 psec) in both the SI-phase and the associated crystalline R-phase [134]. This trap site is identified as the vacant center of the Pauling triacontrahedral clusters (see Figure 2.3(b)).

Positron lifetime measurements [121,122,125] on rapidly solidified Al-Cu-Fe samples indicate the presence of vacancy defects (τ=250-400 psec) (again, in concentrations of 10^{-6}) and a bulk lifetime of ~180-200 psec. On the other hand, the initial investigation of the FCI Al-Cu-Fe quasicrystals prepared by rapid quenching and high temperature annealing [120] indicated that the DB measurements were indistinguishable from those performed on a related crystalline phase in Al-Cu-Fe.

In both systems, the positron lifetime spectra show that the existing defects are stable up to the highest isochronal anneal temperature (450°C for Al-Cu-Fe and 550°C for Al-Cu-Li).

A single crystal of decagonal Al-Ni-Co [126] was studied by both the 2DACAR and positron lifetime techniques. Two lifetimes (τ_1=205 psec, τ_2=385 psec and I_2 ~10%)

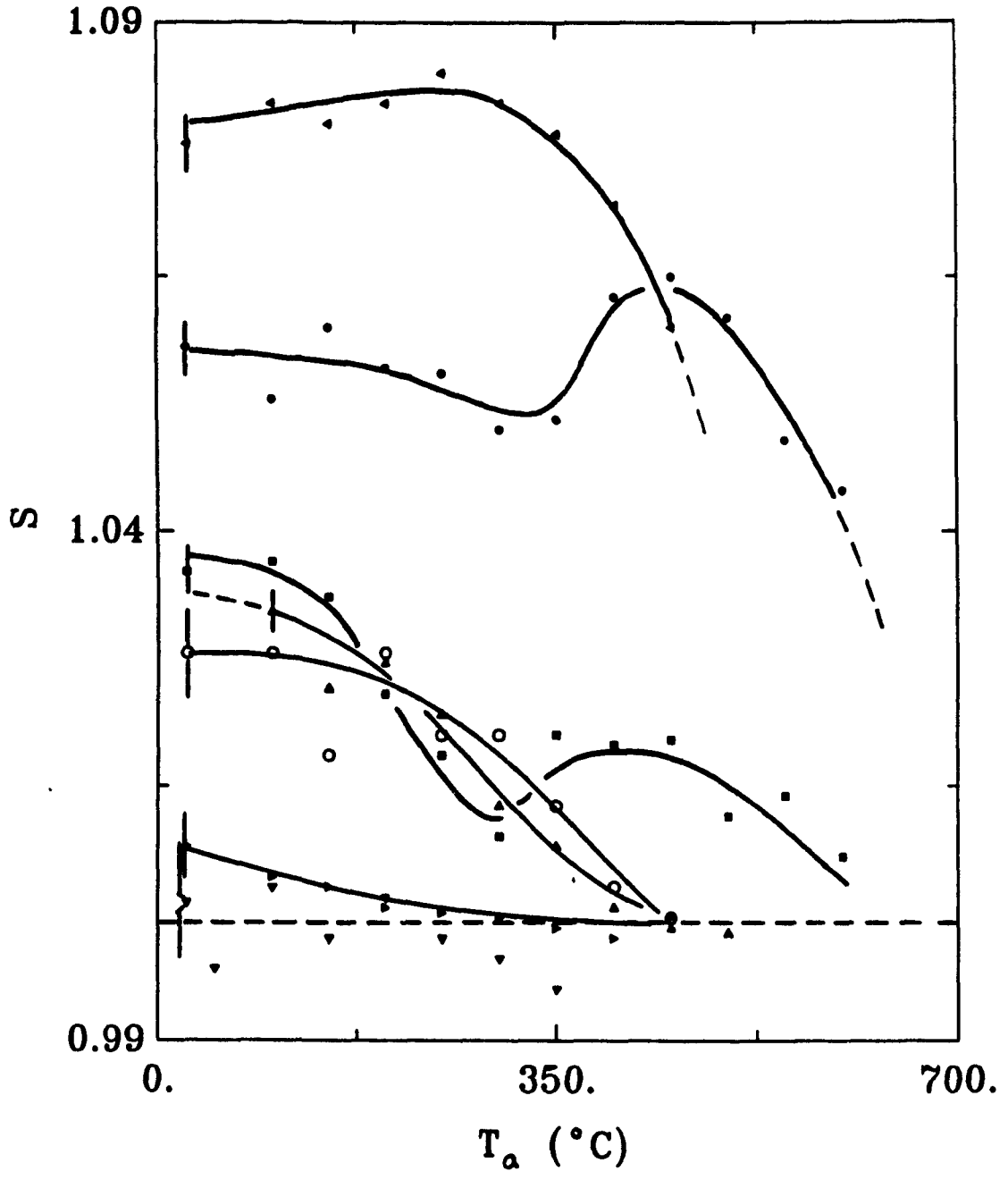

Figure 4.1: Reproduction from published literature of room temperature DB results for as-prepared quasicrystals as a function of isochronal anneal temperature, T_a: (o) Al-Mn [114]; (•) Al-Mn [119]; (■) Al-Mn-Si [115]; (▲) Al-Mn-Si [116]; (◀) Al-Mg-Cu [119]; (▼) Al-Li-Cu [118]; and (▶) Al-Cu-Fe [121]. The S values have been normalized to that (dashed line) obtained from the fully annealed samples.

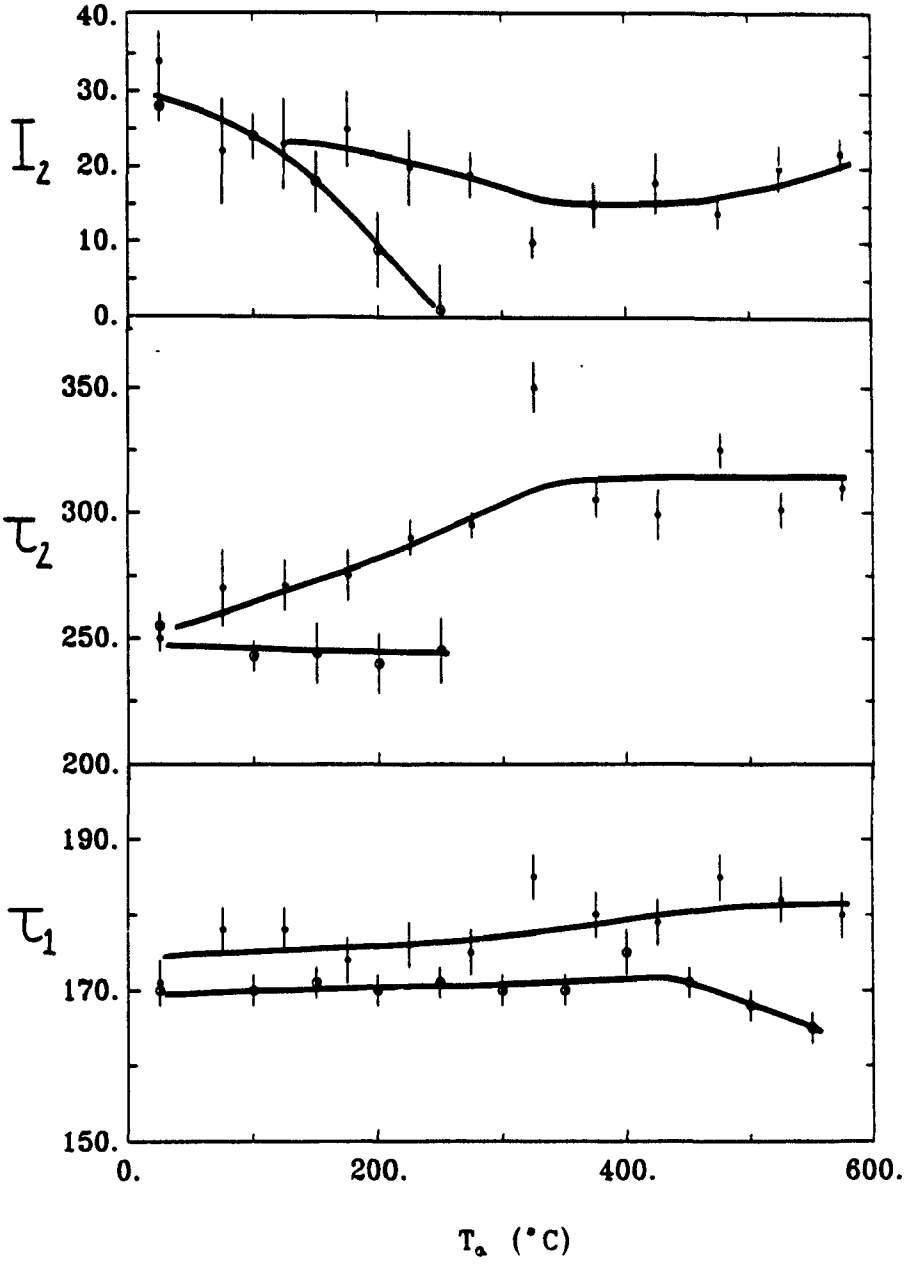

Figure 4.2: Reproduction from published literature of room temperature positron lifetime results for as-prepared quasicrystals as a function of isochronal anneal temperature, T_a:
(o) Al-Mn-Si [115]; and (•) Al-Cu-Fe [125].

were observed, both of which are higher than that expected from annihilations by untrapped positrons. The obvious anisotropy of the structure is not reflected in the 2DACAR measurements giving further indication that the positrons are localized in isotropic traps.

The remaining three entries in Table 4.1 [127,128,131] refer to preliminary studies on Al-Cu-Fe quasicrystalline samples prepared by conventional slow cooling and high temperature annealing. This work constitutes a portion of the material to be presented in chapter 5.

5 Investigation of Al-Cu-Fe FCI quasicrystals

5.1 Introduction

The stable FCI phase in Al-Cu-Fe was the first quasicrystal to be discovered [50,135] with little or no phason disorder (see chapter 2). It is therefore not surprising that it is also the most extensively studied. Structural (e.g. [136,137,138,139,140,141]), thermal (e.g. [142]), electrical (e.g. [54,58,59,143,144,145,146,147,148]), magnetic (e.g. [58,149]) and mechanical [55,57,150] studies have all been reported.

It was not until quite recently, however, that a systematic study [151] of the ternary phase diagram in the vicinity of the FCI phase was performed. The isothermal section at 680°C is reproduced in Figure 5.1. The following general features are observed.

1. The FCI phase is stable and extends over a few atomic percent in composition at elevated temperatures. As the temperature is reduced, this region contracts toward a higher Fe content but remains finite. At room temperature, it is centered on the composition $Al_{62.3}Cu_{24.9}Fe_{12.8}$.

2. At a given stoichiometry, the FCI phase generally transforms upon cooling into a complex mixture of approximant structures characterized by fine diffraction effects (peak broadening, lineshapes, etc.).

The physical properties have also been shown to be highly sensitive to sample composition [143,144] and thermal history [58]. Figure 5.2 shows the variance of electrical conductivity on both the composition and the thermal history of the samples. Thus not only the resulting phase(s) but also the defect structure within that (those) phase(s) are expected to depend quite sensitively upon the details of the sample preparation.

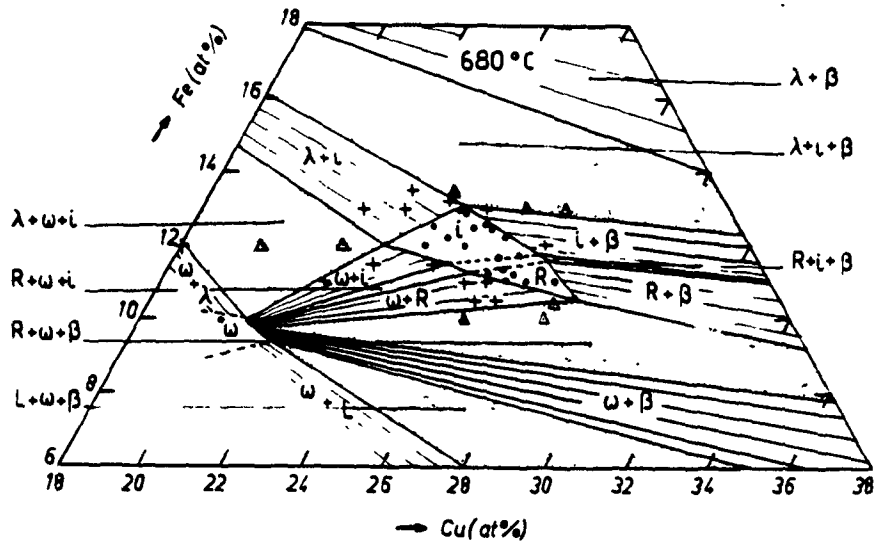

Figure 5.1: Isothermal section at 680°C of the Al-Cu-Fe phase diagram in the vicinity of the FCI phase. The various compositions studied are indicated in the figure (•). i, R, w, λ and β correspond to the FCI, rhombohedral crystalline approximant (a=3.218nm, α=36°), tetragonal $Al_{70}Cu_{20}Fe_{10}$ (space group P4/mnc; a=0.633nm, c=1.481nm), monoclinic $Al_{73}Cu_5Fe_{22}$ (space group C2/m; a=1.5489nm, b=0.80831nm, c=1.2476nm, β=107.72°) and simple cubic Al(Fe,Cu) (space group Pm3m; a=0.29nm) phases, respectively.
Taken from Gratias *et.al.* [151].

In this chapter, results from DB and positron lifetime measurements on a number of Al-Cu-Fe samples as a function of temperature and sample thermal treatment are presented. The chosen stoichiometries and methods of sample preparation reflect those which have been previously reported in the literature. The aim of this work is to: (a) determine the occurrence and behavior of equilibrium defect formation in Al-Cu-Fe FCI quasicrystals; (b) clarify the effect of various thermal treatments on the formation of quenched-in defects; and (c) correlate the defect formation to behavior observed from other studies (i.e. scattering, electron transport, compression testing, etc) which have appeared in the literature.

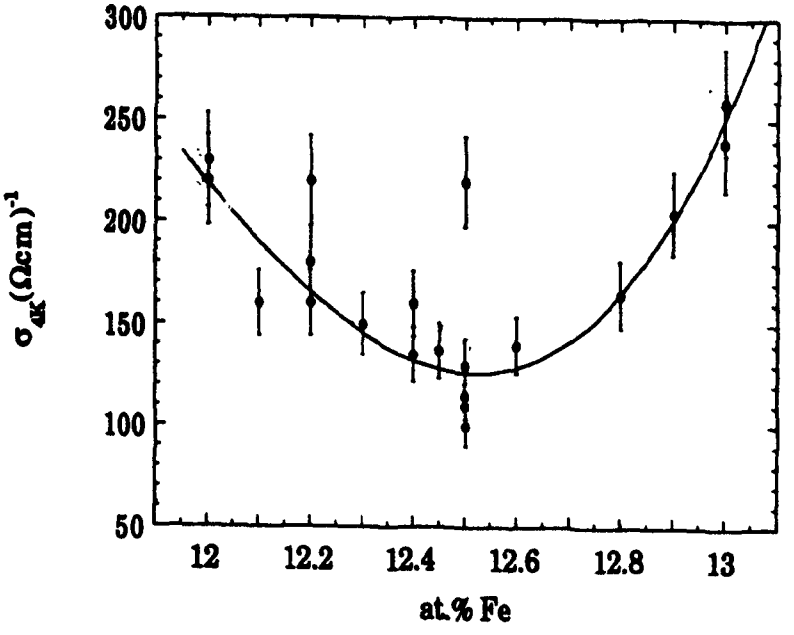

(a)

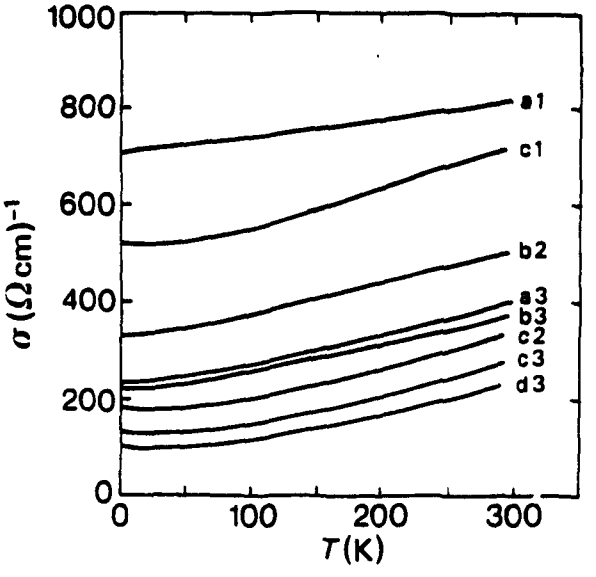

(b)

Figure 5.2: Electrical conductivity, σ, as a function of (a) Fe content and (b) thermal treatment. In (b), the letters correspond to different sample stoichiometries and the numbers correspond to the thermal treatments: a-$Al_{63}Cu_{25}Fe_{12}$; b-$Al_{63}Cu_{24.5}Fe_{12.5}$; c-$Al_{62}Cu_{25.5}Fe_{12.5}$; d-$Al_{62.5}Cu_{25}Fe_{12.5}$; 1-as-quenched; 2-annealed at 600°C; and 3-annealed at 800°C.
(a) and (b) taken from Lindqvist *et.al.* [144] and Klein *et. al.* [58], respectively.

5.2 Experimental details

Polycrystalline samples of nominal stoichiometry $Al_{63}Cu_{25}Fe_{12}$ (sample A), $Al_{62.5}Cu_{25}Fe_{12.5}$ (sample B) and $Al_{62}Cu_{25.5}Fe_{12.5}$ (sample C) were prepared by melting high purity elemental components in an argon arc furnace [1]. The ingots were crushed, sieved through a 120 μm mesh, sealed under argon in quartz tubes and annealed for 24 hours at 800°C. A temperature of 800°C is required to ensure the annealing out of quenched-in impurity phases and residual disorder [58]. The subsequent cooling procedure is discussed below.

Single crystals of $Al_{62}Cu_{22.8}Fe_{15.2}$ [2] (sample D) were prepared by the method described by Ishimasa and Mori [152]. In this case, the above procedure was repeated except that the powdered sample was annealed 12 hours at 870°C followed by slow cooling (<2°C/hour) to 820°C at which the sample was further annealed for 24 hours. The initial anneal stage results in sintering of the powder, whereas compositional inhomogeneities develop in association with the growth of large grains of the FCI phase during the slow cooling. The final anneal stage allows for the removal of quenched-in disorder in the grains. Single crystals (with dimensions of a few mm and masses ranging from 10-20 mg) of the FCI phase were then cut from the ingot.

The stoichiometries of samples A and D are both known to yield stable quasicrystals only at elevated temperatures [142,153]. Slow cooling from such temperatures leads to the production of phason disorder which tends to modulate the structure into complex arrays of microcrystalline particles (see chapter 2). For this reason, samples A and D were ice-water quenched from their final anneal temperature. The stoichiometries of samples B and C correspond closely to that for which the qua-

[1] Typical ingot masses of 3 g resulted in approximately 10 mg of mass loss upon melting. Since the vapour pressure of the Al ($2x10^{-3}$atm) is approximately twice that of Cu and two orders of magnitude that of Fe at 1600°C (just above the melting temperature of Fe), the loss of mass is assumed to be mostly that of Al. This corresponds to about a 0.2 at.% drop in the Al and a 0.1 at.% increase in the Cu and Fe relative compositions, respectively.

[2] The quoted stoichiometry corresponds to that which was determined by Matsuo *et.al.* [149] using an electron probe x-ray microanalyzer. The initial nominal stoichiometry of the ingot was $Al_{66.3}Cu_{20.4}Fe_{13.3}$.

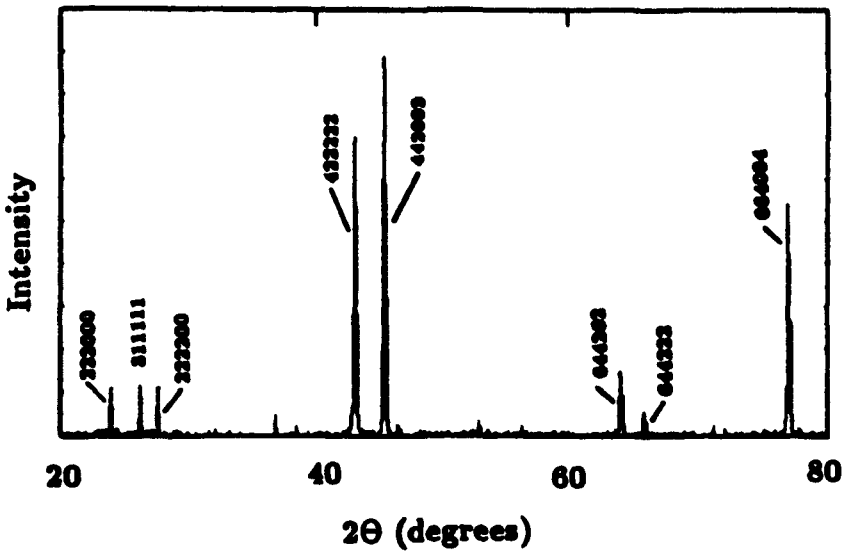

Figure 5.3: Room temperature x-ray powder diffraction spectrum for as-prepared $Al_{62}Cu_{25.5}Fe_{12.5}$ (sample C). All the peaks are indexed to the FCI phase, however, only the principal peaks have been labelled in the figure.

sicrystalline phase is known to be stable over the entire temperature range up to the solidus [142,151]. These samples were therefore slow cooled (<100°C/hour) from their final anneal temperature.

Room temperature x-ray powder diffraction analysis was performed using Cu K_α radiation on a Siemens D-500 scanning diffractometer. A typical diffraction spectrum for the as-prepared samples is shown in Figure 5.3. All four samples showed the existence of a pure FCI phase. In the case of sample D, a single grain cut from the ingot was crushed and the x-ray analysis was performed on the resulting powder.

Room temperature DB and positron lifetime measurements were performed on samples A,B and C after various isochronal anneal treatments. The mass of the single crystal (sample D) was not sufficient to perform the isochronal measurements. Each isochronal anneal [3] was for 12 hours at the temperature, T_a, followed by

[3]The set of anneals on a given sample were done on the entire batch and the subsequent measurements performed on a random portion of it. Before each anneal, the sample was sealed in a quartz tube under a half atm of argon.

either slow cooling (<100°C/hour) or ice-water quenching. A conventional sample/source/sample sandwich geometry was used [127] with the source inserted into a plastic holder with 1 cm x 1 cm x 2.5 mm thick sample compartments. The source was prepared by evaporating ^{22}Na (~fewμCi) onto a 0.011 mm thick sheet of kapton and covering with a second sheet of the same (see chapter 3 for more details). Before each measurement, the samples were sieved to <120μm to ensure constancy of the filling fraction in the sample holder. In all cases, the total mass of sample used was ~750 mg.

The positron source for the *in situ* DB measurements was produced by vacuum sealing approximately 100 mg of the as-prepared samples in quartz followed by thermal neutron irradiation (^{63}Cu(n,γ)^{64}Cu). Typical irradiation times of 10 minutes with a flux of 5.4x10^{-13} neutrons/barn/sec were employed. After a subsequent delay of several hours (to allow for the decay of short-lived activity from ^{28}Al and ^{66}Cu) the sealed samples were inserted into a furnace mounted above the detector on a translational (vertical) stage. Each measurement required 10 minutes, during which, the temperature was controlled to within ±1°C. To compensate for the drop in the ^{64}Cu activity (a typical temperature scan required approximately one full half-life of ^{64}Cu to complete), the sample/detector distance was frequently adjusted (see chapter 3 for more details).

All the measurement results reported in the next section were confirmed by repeating the experiments on a second batch of samples prepared by the identical procedures.

5.3 Results

Results from the isochronal DB and positron lifetime experiments are given in Figure 5.4 and Tables 5.1 and 5.2. The evolution of the x-ray powder diffraction peak shapes as a function of the thermal treatment is illustrated in Figure 5.5 for sample A.

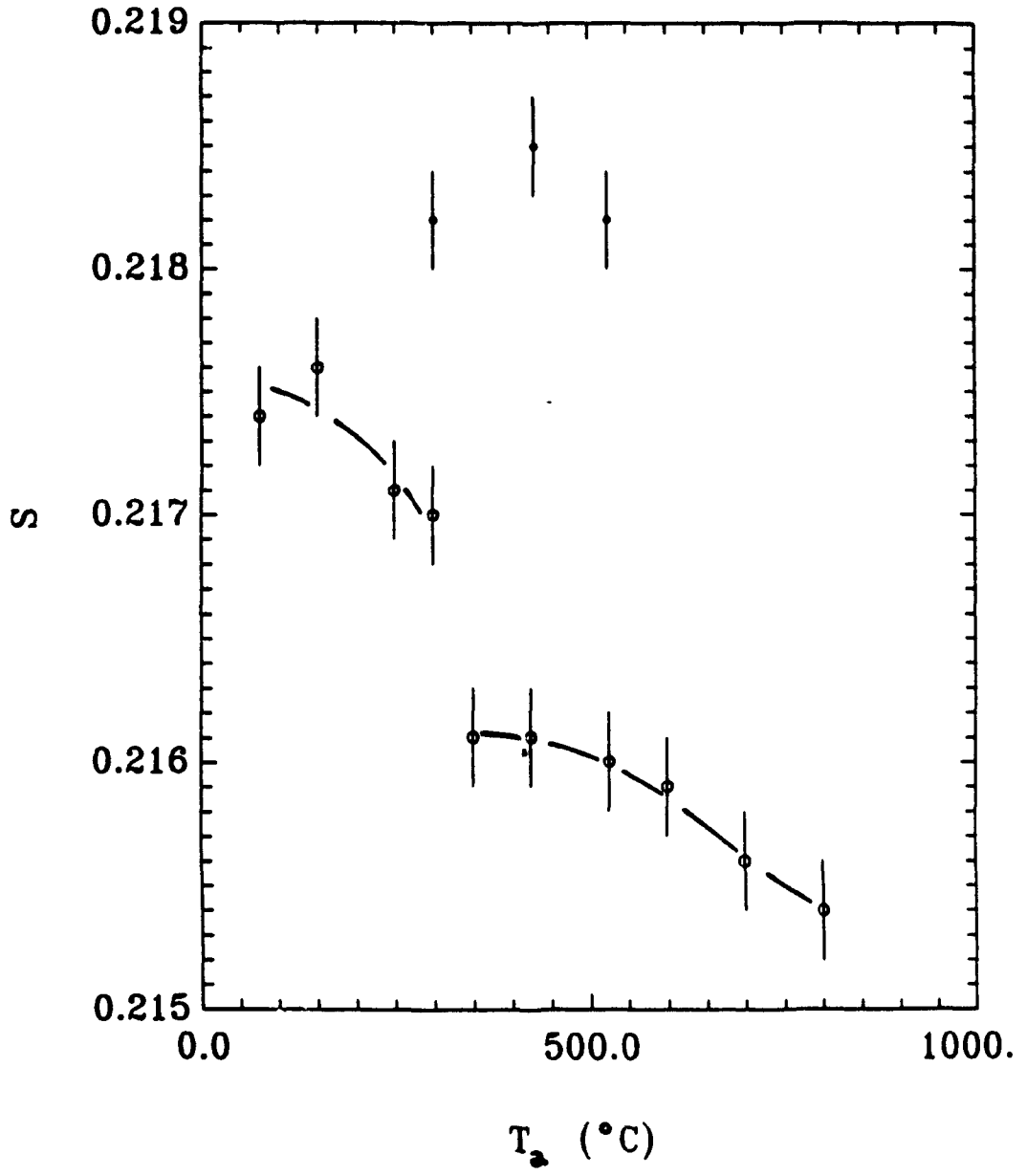

Figure 5.4: S parameter values for $Al_{63}Cu_{25}Fe_{12}$ (sample A) measured at room temperature after annealing at T_a followed by either ice-water quenching (o) or slow cooling (•). The curve drawn through the points is only a guide and does not represent a fit to a model.

sample	T^* [°C]	S parameter value IWQ $> T^*$	IWQ $< T^*$	slow cooled
$Al_{63}Cu_{25}Fe_{12}$ (sample A)	300-350	0.2158(4)	0.2174(4)	0.2182(4)
$Al_{62.5}Cu_{25}Fe_{12.5}$ (sample B)	-	0.2126(2)		0.2129(2)
$Al_{62}Cu_{25.5}Fe_{12.5}$ (sample C)	-	0.2124(2)		0.2124(2)

Table 5.1: Summary of isochronal anneal DB results. T^* denotes the transition temperature from the ice-water quenching (IWQ) experiments corresponding to a large change in the S parameter value. The uncertainties in S are a reflection of the spread in values obtained in the indicated temperature range.

Figures 5.6 and 5.7 show L as a function of temperature from *in situ* DB measurements on all four samples.

The bulk lifetime, τ_b (i.e. the lifetime expected for a defect-free sample), and defect concentration, c, were calculated assuming a simple two-state trapping model [4] (see e.g. [94]) using

$$\tau_b = \tau_1\tau_2/(\tau_1 I_2 + \tau_2 I_1) \tag{5.1}$$

and

$$c = (I_2/\mu)(\tau_1^{-1} - \tau_2^{-1}), \tag{5.2}$$

respectively. I_1 and I_2 are the relative intensities of the components with lifetimes τ_1 and τ_2, respectively. τ_2 corresponds to the longer lived (vacancy) component. The specific trapping rate, μ, was taken to be $\sim 10^{15}$/sec which is typical for vacancies [154]. The approximate size of the vacancy, N, was determined from a comparison of the difference, τ_2-τ_b, with that found for Al [155].

A typical deconvoluted DB annihilation spectrum is given in Figure 5.8 along with least-squares fits (see chapter 3) to the simple metal model (i.e. a superposition of a parabola and a gaussian) and to two gaussians.

The following general features are observed.

[4]The positrons are assumed to annihilate from either the non-localized bulk state or from a localized trap state. It is further assumed that the positron can not de-trap from the localized state.

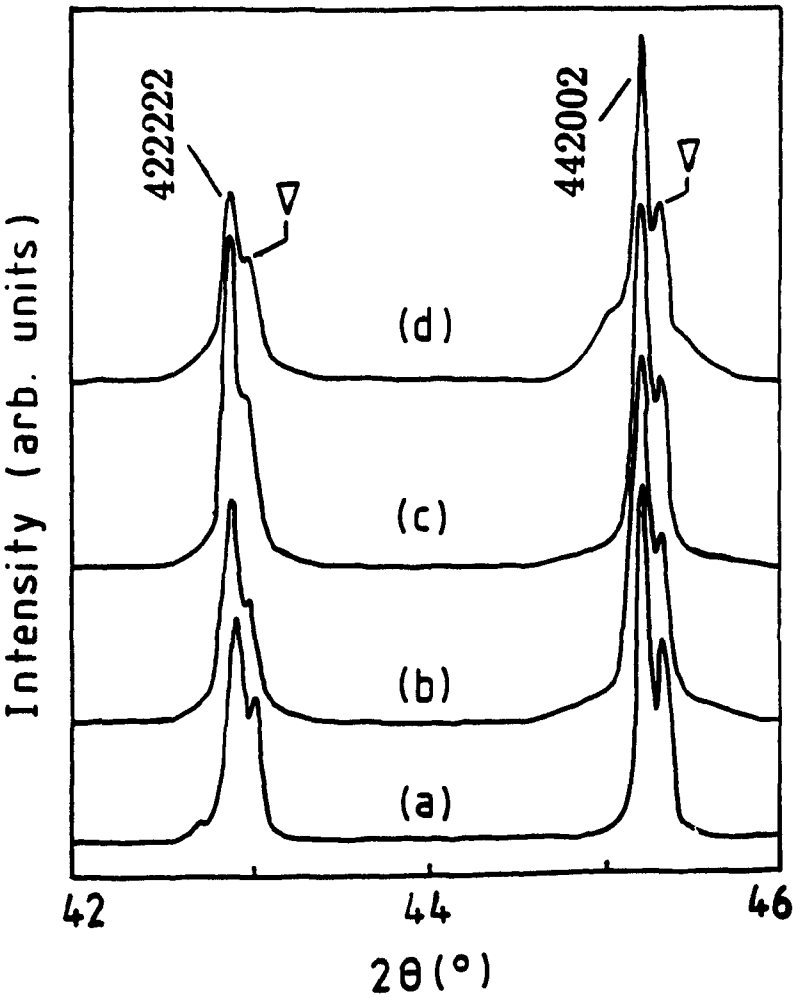

Figure 5.5: Room temperature Cu K_α x-ray powder diffraction spectra for $Al_{63}Cu_{25}Fe_{12}$ (sample A) ice-water quenched from (a) 800°C, (b) 525°C, (c) 165°C and slow cooled from (d) 525°C. (∇) indicates the presence of Cu $K_{\alpha 2}$ lines.

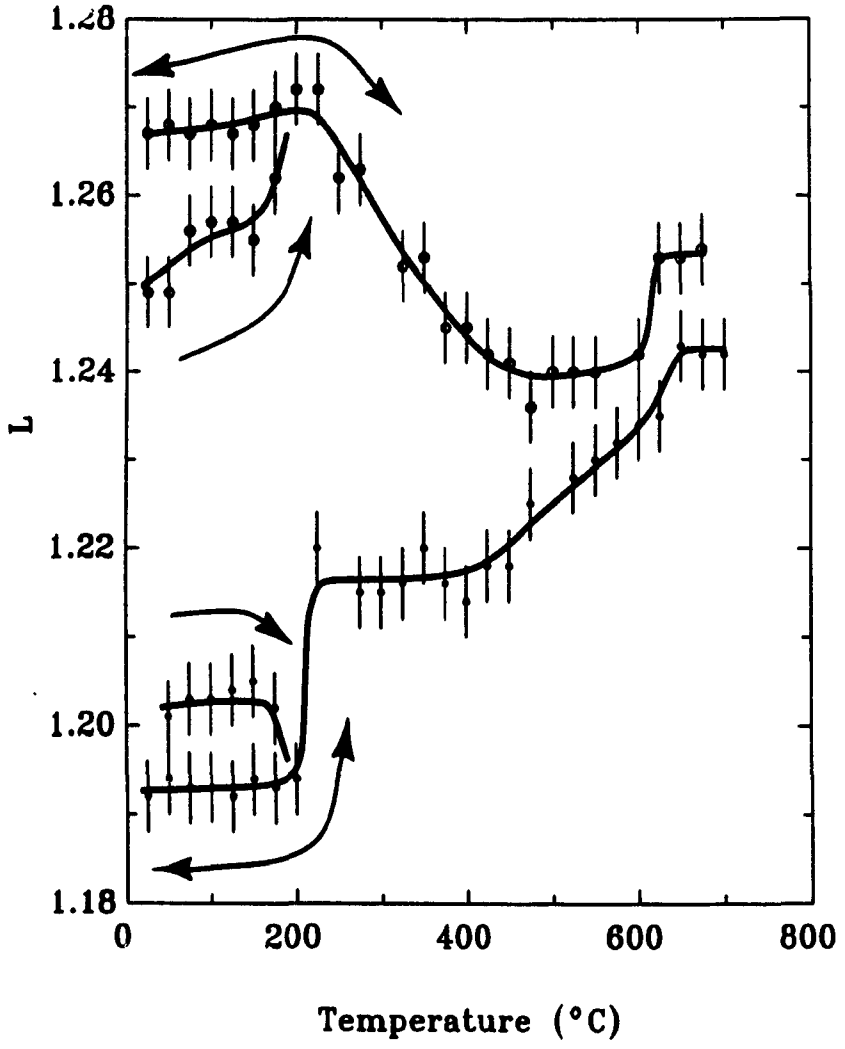

Figure 5.6: L parameter values from *in situ* DB measurements on polycrystalline (o) $Al_{63}Cu_{25}Fe_{12}$ (sample A) and (•) $Al_{62}Cu_{25.5}Fe_{12.5}$ (sample C). The lines drawn through the points are only guides and do not represent fits to a model. The single headed arrows correspond to the initial heating whereas the double headed arrows correspond to subsequent thermal cycling.

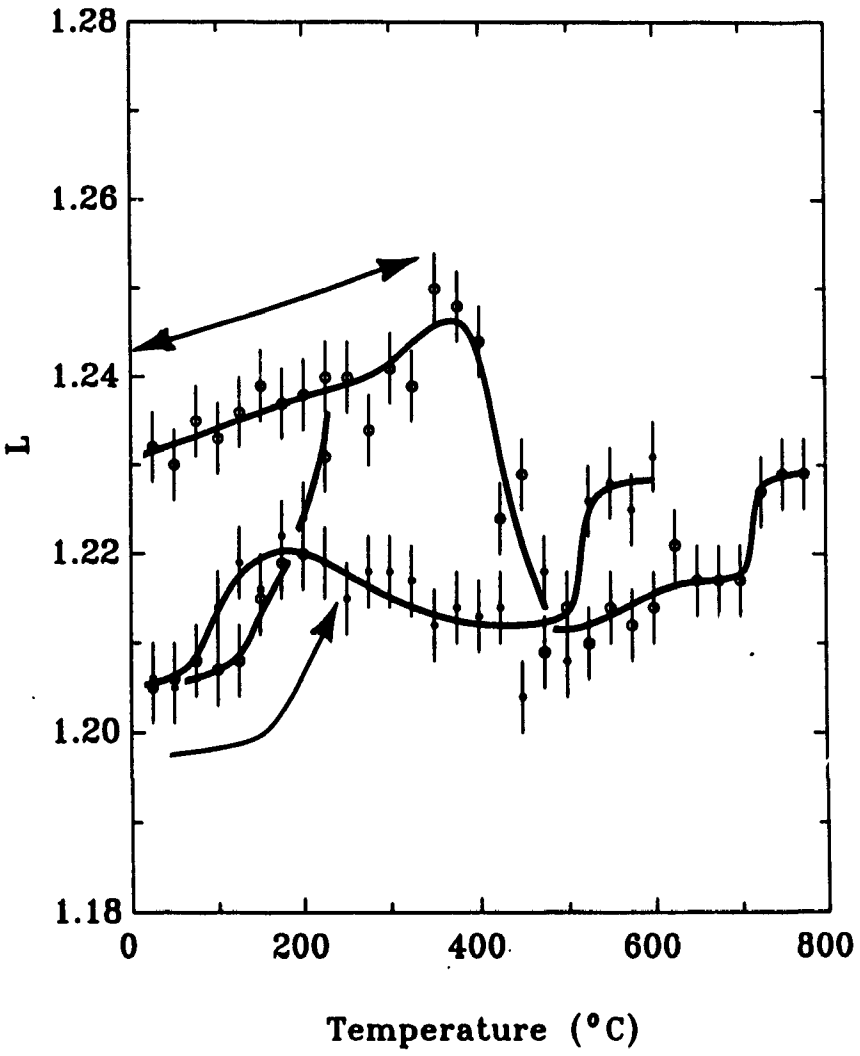

Figure 5.7: L parameter values from *in situ* DB measurements on single crystal (o) $Al_{62}Cu_{22.5}Fe_{15.2}$ (sample D) and polycrystalline (•) $Al_{62.5}Cu_{25}Fe_{12.5}$ (sample B). The lines drawn through the points are only guides and do not represent fits to a model. The single headed arrow corresponds to the initial heating whereas the double headed arrow corresponds to subsequent thermal cycling.

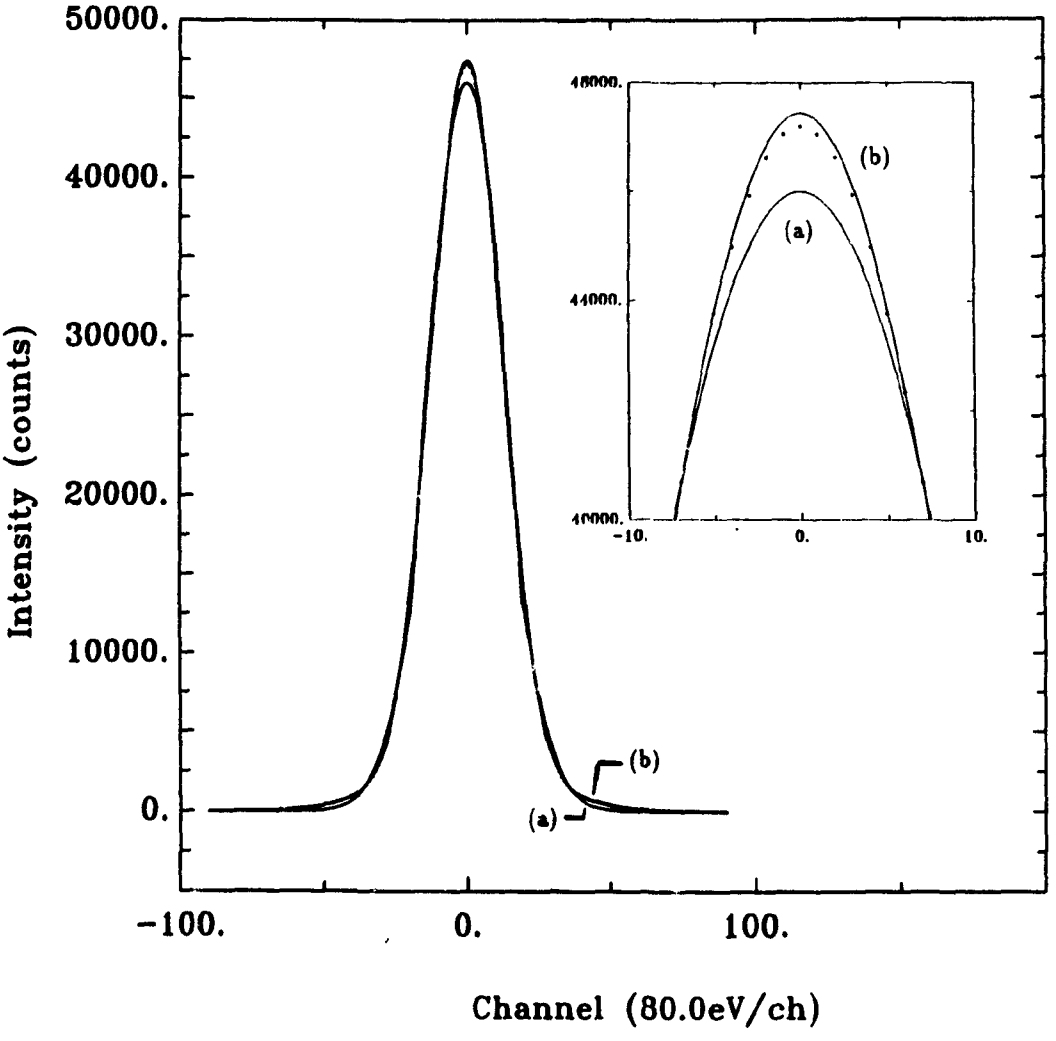

Figure 5.8: Direct space deconvoluted room temperature DB annihilation spectrum for $Al_{62}Cu_{25.5}Fe_{12.5}$ (sample C). Also included in the figure are least-squares fits to a superposition of: (a) a parabola and a gaussian; and (b) two gaussians. The inset shows a magnified view of the peak centroid region.

treatment	$\overline{\tau}$ [psec]	τ_1 [psec]	τ_2 [psec]	I_2 [%]	τ_b [psec]	VOF	N	c [ppm]
			$Al_{63}Cu_{25}Fe_{12}$ (sample A)					
SC200°C	214(2)	196(2)	403(10)	21(5)	220(2)	1.1	>2	2
SC530°C	214	195	393	21	218	1.2	>2	2
IWQ530°C	206	193	300	10	200	1.2	2	<1
			$Al_{62.5}Cu_{25}Fe_{12.5}$ (sample B)					
SC200°C	195	190	227	15	195	1.3	1	1
SC530°C	190	181	242	19	190	1.2	1	1
IWQ530°C	198	192	235	15	197	1.2	1	<1
			$Al_{62}Cu_{25.5}Fe_{12.5}$ (sample C)					
SC200°C	194	194	-	-	194	1.0	-	-
SC530°C	190	180	270	18	191	1.2	1	1
IWQ530°C	196	193	237	8	196	1.0	1	<1

Table 5.2: Results from one and two component fits to Al-Cu-Fe positron lifetime spectra corrected for source contributions. All thermal treatments involved annealing at the specified temperatures for 12 hours followed by either slow cooling (SC) or ice-water quenching (IWQ). $\overline{\tau}$ is the mean lifetime and I_2 is the relative intensity of the second lifetime component, τ_2, in the two component fit. τ_b is the calculated bulk lifetime (see text), VOF is the variance-of-fit value, N is the estimated size of the vacancy in terms of monovacancies and c is the calculated vacancy concentration.

1. An increase in S is observed below about 350°C from the isochronal anneal measurements on sample A. Samples B and C do not show this behavior (see Figure 5.4 and Table 5.1).

2. Assuming a simple two-state trapping model, vacancy concentrations up to a few parts per million (ppm) are calculated for the samples (see Table 5.2). This is consistent with previously reported results [129].

3. A broad peak in the temperature dependence of L is observed for samples A and D extending from room temperature to about 450°C. The lifetime measurements (see Table 5.2) on sample A show that the elevation in L corresponds to an increase in both τ_2 and I_2.

4. A broad peak in the temperature dependence of L is also observed for sample B (see Figure 5.7), although the elevation in L is not as great as for samples A and D. No significant change in either τ_2 or I_2 (see Table 5.2) can be observed to correspond to the elevation in L.

5. For sample C no such peak is observed. Instead, a step occurs at about 225°C (see Figure 5.6). Lifetime measurements on the sample after annealing and quenching from above and below this step show that the elevation in L corresponds to the generation of a second component with a lifetime (τ_2) of ~250 psec (see Table 5.2).

6. Non-equilibrium behavior is observed in the as-prepared states of samples A, C and D (see Figures 5.6 and 5.7). Reversion to equilibrium (i.e. reversible) behavior is observed after heating the samples above ~200°C.

7. In all four samples, a high temperature step is observed for L between about 525°C and 750°C depending upon the stoichiometry (see Figures 5.6 and 5.7).

8. The deconvoluted DB annihilation spectra are not well described by a simple metal model (i.e. free electron component). The valence electron contribution is roughly gaussian in shape (see Figure 5.8). The relatively small change in L as a function of temperature does not lead to an unambiguous (i.e. statistically significant) correlated change in the deconvoluted spectra.

5.4 Discussion

The existence of two components in the positron lifetime spectra has been interpreted in previous studies by other workers [121,122,125,129] in terms of the simple two-state trapping model. The positrons are assumed to annihilate from either the bulk state (τ_1) or a localized state from within a vacancy (τ_2). This interpretation was used to calculate the vacancy concentrations for the present data (see Table 5.2). The results

are consistent those reported previously [121,129]. However, no justification has been given for a bulk lifetime, τ_b, of ~195 psec in FCI Al-Cu-Fe quasicrystals.

There is now considerable evidence (e.g. [64,144,156]) to support the suggestion that the stable FCI quasicrystals are electron compounds (i.e. Hume-Rothery compounds). Interaction of the Fermi surface with a pseudo-zone formed by a set of Bragg planes (corresponding to the most intense x-ray Bragg peaks: 422222 and 442002 in Figure 5.3), implies

$$2k_F \sim G \tag{5.3}$$

where k_F and G are the magnitudes of the Fermi wavevector and reciprocal lattice vector, respectively. Assuming a spherical Fermi surface,

$$k_F = (3\pi^2 n_e)^{1/3} \tag{5.4}$$

where $n_e = (e/a)n_a$ is the electron density and n_a is the atomic density. Since the mass density of the Al-Cu-Fe quasicrystals has been determined to be ~4.5 g/cm^3 [64] and G = 3.094 Å^{-1} [5] for $Al_{62}Cu_{25.5}Fe_{12.5}$ (sample C), n_e =1.25x10^{23} cm^{-3}, and e/a = 1.84 electrons/atom. Note that this e/a value is close to 1.78 electrons/atom which is calculated on the basis of a valence of +3, +1 and -2.66 (Pauling charge transfer [157]) for Al, Cu and Fe, respectively.

In electrically conductive materials, an upper limit of τ_∞ ~500 psec (=$1/\lambda_\infty$) (irrespective of whether the positrons annihilate from within a vacancy or not) results from a weighted average of the annihilation rates of para- and ortho-positronium. This implies that [158]

$$\tau_b = [\lambda_\infty(1+\lambda)]^{-1}. \tag{5.5}$$

A recent consideration of the systematic variation of τ_b in alkali metals and poly-

[5]The value of G = 3.094 Å^{-1} is calculated from a weighted average of the reciprocal vectors, G_{422222} (=2.9856 Å^{-1}) and G_{442002} (=3.1381 Å^{-1}), corresponding to the 422222 and 442002 x-ray powder diffraction peaks in Figure 5.3. The weighting corresponds to the multiplicity of the Bragg planes: 12 planes normal to the 5-fold axes of the icosahedron for the 422222 peak; and 30 planes oriented along the 2-fold edges of the icosahedron for the 442002 peak. Thus G = $(12/42)G_{422222} + (30/42)G_{442002}$.

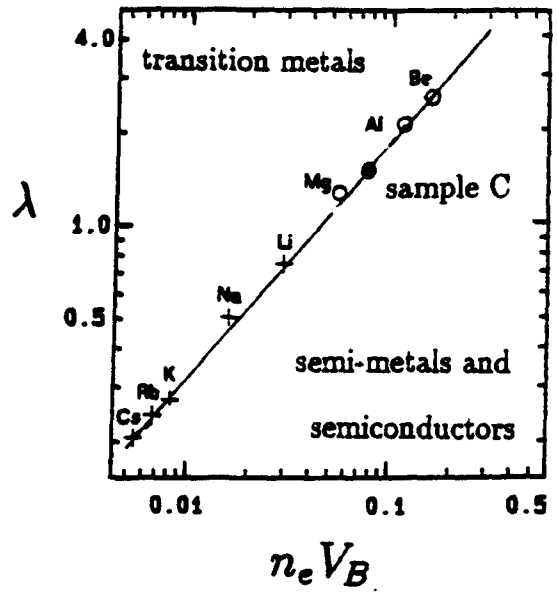

Figure 5.9: Bulk annihilation rates, λ, for the alkali metals (+) and the polyvalent metals without d-electrons (o) versus $n_e V_B$. The solid line represents expression 5.6. Also included in the figure is the result for $Al_{62}Cu_{25.5}Fe_{12.5}$ (sample C) (•).

valent metals without d-electrons has resulted in the empirical relation [112],

$$\lambda = (22.6 n_e V_B)^{0.78}, \tag{5.6}$$

where $V_B = 4\pi a_B^3/3$ and a_B is the Bohr's radius (=5.292x10^{-11} m). The bulk annihilation rates are plotted in Figure 5.9 with respect to $n_e V_B$. As can be seen in the figure, a line representing expression 5.6 is in very good agreement with the data.

Expression 5.6 for sample C gives τ_b=196 psec which is in good agreement with the experimentally determined value (see Figure 5.9). In general, transition metals tend to fall above this line while semi-metals and semiconductors tend to fall below this line. This indicates that τ_1 from the positron lifetime fits corresponds to positron annihilation with the conduction electrons (i.e. not the d-electrons).

The deconvoluted DB spectra tend to support this result. The addition of a second gaussian to the simple metal model (see chapter 3) would account for a d-electron contribution to the distribution [159]. However, the spectra were found to fit best

(although not exactly) with a single gaussian for the valence electron contribution (see Figure 5.8). Unfortunately, the uncertainty regarding the incomplete deconvolution does not allow for a precise determination of the valence electron energy distribution.

This result is incompatible with the previous assumption that the positrons are primarily in an extended state at the time of annihilation. If this were the case, the significant d-orbital character of the Al-Cu-Fe FCI quasicrystals would influence the annihilation parameters.

The explanation is that the positrons are highly localized in Al-rich regions of the atomic structure. This would exclude overlap of the positron wavefunction with those of the Cu and Fe d-electrons. The most likely candidate for such sites are vacant cluster centers (see chapter 2) surrounded by an icosahedral coordination of Al atoms. The stability of the τ_1 value over varying stoichiometry and thermal treatment (see Table 5.2) lends further support for the suggestion that the sites are intrinsic structural vacancies.

The observation of a single lifetime component in sample C indicates that saturation trapping of the positrons occurs within these intrinsic structural vacancies. The simple two-state trapping model is not applicable.

Figures 5.6 and 5.7 and Table 5.2 clearly illustrate the need for care when reporting the thermal history of the sample under investigation (e.g. compare the results from the initial heating of the as-prepared samples to that from subsequent thermal cycling). In particular, slow cooling (<100°C/hour) sample C still resulted in quench-in vacancy disorder (as evidenced by elevated L, I_2 and τ_2 values). In each case, the non-equilibrium behavior is removed after annealing the sample at ~200°C.

The positron annihilation measurements show that equilibrium vacancies are present in the Al-Cu-Fe samples over the entire temperature range investigated. In fact, only below about 200°C for sample C was there a failure to observe a second lifetime component.

There is no doubt that the longer-lived τ_2 is associated with the formation of an open volume defect. The significant variance in both I_2 and τ_2 indicates that the

Sample	T_{cryst} [°C]	$T_{plastic}$ [°C]
$Al_{63}Cu_{25}Fe_{12}$ (sample A)	425-450	600-630
$Al_{62.5}Cu_{25}Fe_{12.5}$ (sample B)	-	525-550
$Al_{62}Cu_{25.5}Fe_{12.5}$ (sample C)	-	625-640
$Al_{62}Cu_{22.8}Fe_{15.2}$ (sample D)	425-450	725-750

Table 5.3: Temperature regimes for crystalline phase formation ($< T_{cryst}$) and plasticity ($> T_{plastic}$) as observed by the *in situ* Doppler broadening measurements.

second positron lifetime component does not correspond to an intrinsic structural vacancy. It is possible that τ_2 can be ascribed to a distortion of a fraction of the intrinsic vacancies or to the formation of a distinct form of defect. The correct interpretation is likely to be sample specific.

Both the isochronal and *in situ* DB measurements show an elevation of the lineshape parameter as the temperature is lowered (see Figures 5.4, 5.6 and 5.7). This can be associated with the instability of the FCI quasicrystalline phase in samples A and D. Positron lifetime measurements on sample A (Table 5.2) show that this corresponds to an increase in I_2 and τ_2 to about 20% and 400 psec, respectively. It should be noted, however, that the isochronal anneal experiment indicates a crystallization temperature for sample A of 300°C-350°C (Table 5.1) whereas the *in situ* experiment gives 425°C-450°C (Table 5.3).

This discrepancy can be explained in one of two ways. Ice-water quenching from above the crystallization temperature, T_{cryst}, may be only partially successful at preventing the transformation process. Evidence for this comes from the relatively high value for L at room temperature for the as-prepared sample A compared to that above T_{cryst} (Figure 5.6). Thus only after annealing below 350°C does the transformation progress far enough to result in an elevation of S (and L) above that from ice-water quenching the sample from higher temperatures. Alternatively, the long anneal times for the isochronal experiments may allow for a more complete

progression of the transformation to the FCI phase at lower temperatures.

It has been shown that the microcrystalline morphology of the transformed phase consists of oriented grains [160,161] with dimensions of less than a few hundred angstrōms [162]. Such a transforma'·on results in the appearance of diffuse scattering and low intensity shoulder peaks about the principal powder diffraction peaks of the FCI phase (see e.g [162]). Figure 5.5 reveals these same features in the case of sample A. It is therefore concluded that the positrons are becoming trapped at the microcrystallite boundaries.

The precise nature of these boundary-trap sites is not known. High resolution electron microscopy (HREM) studies [160,162] have indicated that the interfacial regions are coherent, eliminating the prospects of microvoid formation. On the other hand, the pronounced temperature dependence of L for the microcrystalline phase (samples A and D in Figures 5.6 and 5.7, respectively) suggests that the traps are extended in one or more dimensions [163].

The stoichiometries of sample B and C have been shown to produce a stable FCI quasicrystal over the entire temperature range up to the solidus. The absence of a pronounced elevation in S, L and τ_2 for low temperature anneals (see Figures 5.4, 5.6, 5.7 and Tables 5.1 and 5.2) confirms this result.

The second component lifetime, $\tau_2 \sim 240$ psec, found for both sample B and C is significantly lower than that observed in samples A and D. Furthermore, it appears for sample C only after annealing above $\sim 200°C$ and does not induce a noticeable change in the x-ray powder diffraction spectra. This implies the existence of a positron-trap site other than the extended inter-grain site found for the microcrystalline phase.

It is not likely that a vacancy cluster, large enough to produce a $\tau \sim 240$ psec (the intrinsic structural vacancy, with $\tau \sim 195$ psec, is expected to be approximately a monovacancy in size), would be thermally generated at 200°C. A least-squares fit of the low temperature L values for sample C to expression 3.9 is shown in Figure 5.10. The enthalpy of vacancy formation is determined to be 0.6-0.8 eV.

Time-of-flight quasi-elastic neutron scattering experiments have recently been per-

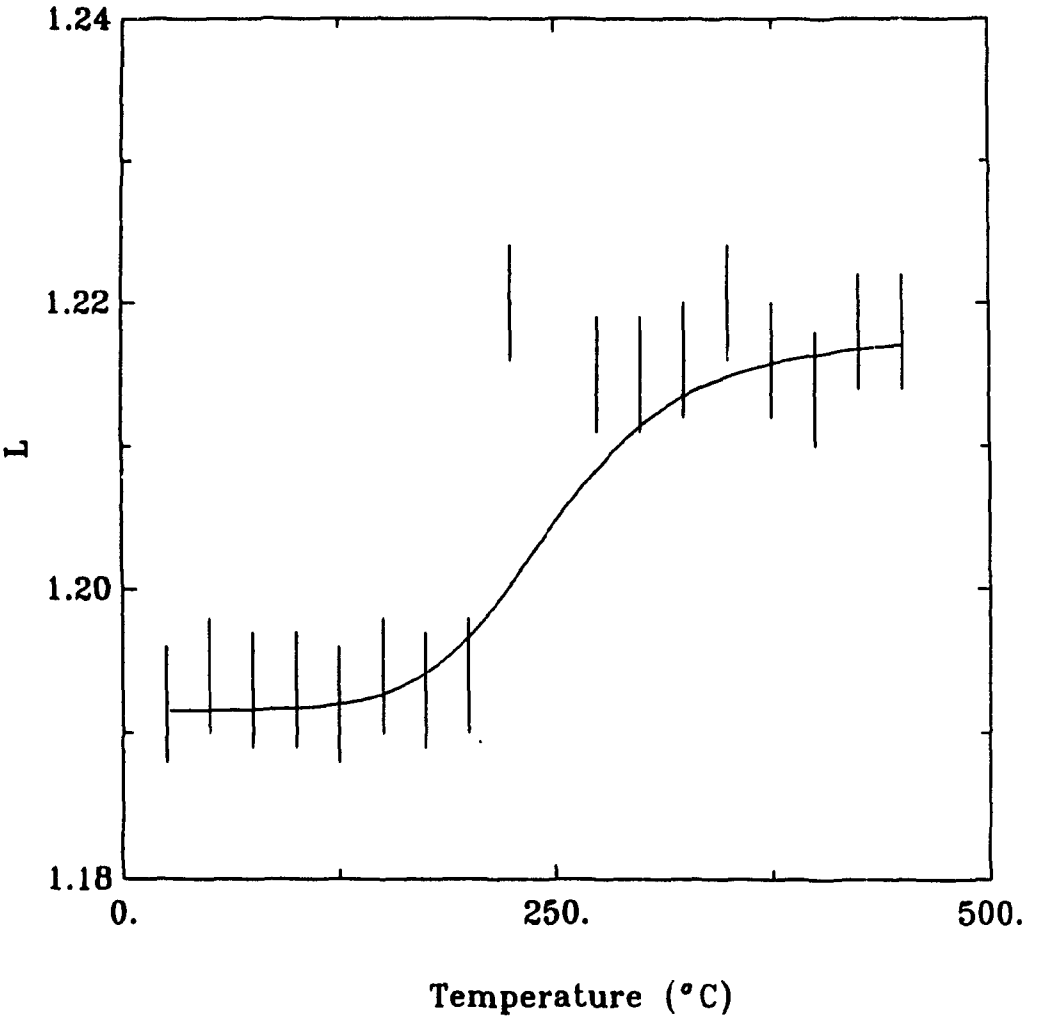

Figure 5.10: The L values in the vicinity of the low temperature step from *in situ* DB measurements on $Al_{62}Cu_{25.5}Fe_{12.5}$ (sample C). The curve corresponds to a least-squares fit to expression 3.9.

formed as a function of temperature on an $Al_{62}Cu_{25.5}Fe_{12.5}$ sample [164,165,166]. Broadening of the quasi-elastic component occurs above 650°C. This effect has been ascribed to cooperative phason hopping of Al and Cu atoms. The participating Cu atoms are presumed to occupy a fraction of the atomic cluster centers (see chapter 2) from which a phason hop to an unoccupied site beyond the inner icosahedral shell of Al atoms occurs. This process is assisted by a cooperative phason hop of an Al atom from the icosahedral shell to its alternate site within a double well potential [164]. The Al phason thus acts as a de-pinning mechanism for the Cu phason with a measured de-pinning energy of 0.75 eV.

It is therefore likely that the observed steps in the L value for sample C at ~200°C and ~ 640°C correspond to the activation of dynamic Al and Cu phasons, respectively. Displacement of an Al atom would open up the close-packed icosahedral shell, distorting the intrinsic structural vacancy. This would further localize the positron wavefunction within a deeper potential well, decreasing the integrated positron/electron wavefunction overlap and thus increasing the positron lifetime. It should be noted that the increase in the positron lifetime (~ 45 psec) is close to that observed for a divacancy compared to a monovacancy in Al [167].

Evidently the failure to observe a low temperature step for L in sample B implies that static phason disorder is locked into this sample at room temperature.

The observation of a high temperature step in L for all four samples (525°C< T <750°C) indicates that a similar dynamic Cu phason occurs in each. However, the reason for the dependence of the step temperature on sample stoichiometry is not known.

A further comparison can be made to the results from recent compression tests [57] on Al-Cu-Fe FCI quasicrystals which show a brittle-to-plastic transformation. In the case of sample A, the step temperature occurs between 600°C and 630°C which corresponds well to the reported temperature of 604°C for the onset of plasticity, $T_{plastic}$ [57] (for a sample with the same stoichiometry). Any change in the structure responsible for the plasticity is expected to correspond to a significant change in the

defect structure. This should be observed in the positron measurements. Since no other anomaly is observed in the temperature dependence of L (in the temperature region of interest), this step must correspond to $T_{plastic}$. The temperature regimes, derived from Figures 5.6 and 5.7, corresponding to activation of the dynamic Cu phason and hence phase plasticity, $> T_{plastic}$, are summarized in Table 5.3.

5.5 Conclusions

Equilibrium vacancy formation and behavior in Al-Cu-Fe FCI quasicrystals have been identified and categorized according to observed features from electron microscopy, x-ray diffraction, neutron scattering and compression testing studies.

A quasicrystal-to-microcrystalline phase transition has been observed in $Al_{63}Cu_{25}Fe_{12}$ and $Al_{62}Cu_{22.8}Fe_{15.2}$ indicating that the FCI phase is stable only at elevated temperatures for these stoichiometries. A fraction of the positrons are trapped in extended regions within the coherent grain boundaries of the microcrystalline phase. A positron lifetime of 300-400 psec results.

In both cases, the FCI phase can be quenched-in at room temperature. Reversion to the equilibrium microcrystalline phase can be accomplished by annealing the quenched samples at ~200°C.

The FCI phase in $Al_{62}Cu_{25.5}Fe_{12.5}$ and $Al_{62.5}Cu_{25}Fe_{12.5}$ is found to be stable down to room temperature.

Both the FCI phase and the microcrystalline phase possess an intrinsic structural vacancy corresponding to the vacant center of an icosahedral shell of Al atoms. This site forms a saturation trap for the positrons with a resulting positron lifetime of ~195 psec.

Thermal activation of two types of dynamic phasons, one involving atomic hops of Al atoms and the other involving Cu atoms, have been observed in the FCI phase. The Al phasons are activated at ~200°C and the Cu phasons are activated within the temperature range, 525°C-750°C, depending upon the sample stoichiometry. The

Al phasons distort the intrinsic structural vacancy increasing the trapped positron lifetime to ~240 psec.

The FCI phase is observed to possess a brittle-to-plastic transformation upon heating. The onset temperature coincides with the activation of the dynamic Cu phasons.

6 Synopsis and future prospects

The results presented in this thesis from positron annihilation experiments on Al-Cu-Fe FCI quasicrystals impact upon the published literature in two ways.

Prior to this work, three groups, Chidanbaram *et. al.* [121,129], Howell *et. al.* [122] and Kristiakova *et. al.* [125], had published results from room temperature positron annihilation measurements on Al-Cu-Fe FCI quasicrystals. In all three cases, the principal positron lifetime (180-200 psec) was incorrectly ascribed to a positron which was untrapped at the instant of annihilation. This lead to confused interpretations of the positron results. In particular, Chidanbaram *et. al.* had claimed that the absence of a saturation trap site and the presence of a persistent long-lived second component to the lifetime spectra were justification for the applicability of an icosahedral glass model for the Al-Cu-Fe FCI structure. This is clearly at odds with numerous microscopy and diffraction studies which have shown the Al-Cu-Fe FCI structure to be virtually free of phason disorder.

The present work has demonstrated the incorrectness of the interpretation of these previously published results and verified the basic results regarding the Al-Cu-Fe FCI structural details derived from other experimental techniques.

The *in situ* DB measurements represent the first study of the equilibrium defect behavior in quasicrystals as a function of temperature. In addition to verifying the instability of the Al-Cu-Fe FCI phase in some of the stoichiometries, new results, not seen previously by other techniques, have been reported. Most notably, the observation of the thermal activation of dynamic Al and Cu phasons and in the latter case, its connection to the onset of plasticity in the FCI phase.

The results presented in this thesis were restricted to the FCI phase in Al-Cu-Fe. Successful interpretation of the positron annihilation data invariably requires direct comparison of the results with those from complementary experiments. Other well

ordered and stable quasicrystals are known to exist in, for example Al-Cu-Co, Al-Cu-Ru and Al-Cu-Os (and other, non-Al-Cu-based materials). However, the present dearth of published results for these materials would likely preclude a repetition of the success experienced here for the interpretation of the Al-Cu-Fe positron annihilation data. However, there is no doubt that this situation will be rectified in the near future.

A Appendix: Nuclear decay schemes

Figures A.1 and A.2 illustrate the nuclear decay schemes for the two positron-emitting isotopes, ^{22}Na and ^{64}Cu, employed as positron sources in this thesis work. Figure A.3 illustrates the nuclear decay scheme for the calibration source, ^{103}Ru.

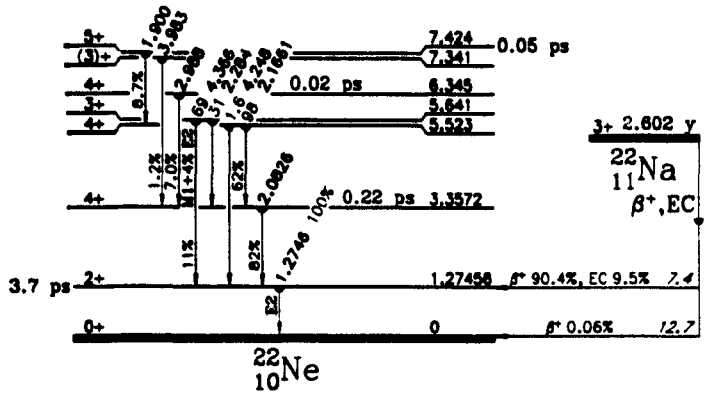

Figure A.1: Decay scheme for ^{22}Na.
Adapted from Ref.[168].

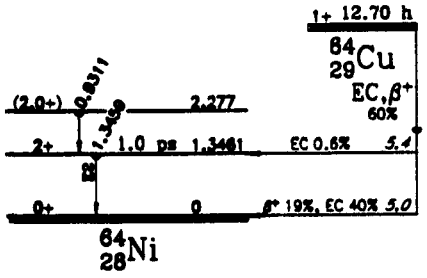

Figure A.2: Decay scheme for ^{64}Cu.
Adapted from Ref.[168].

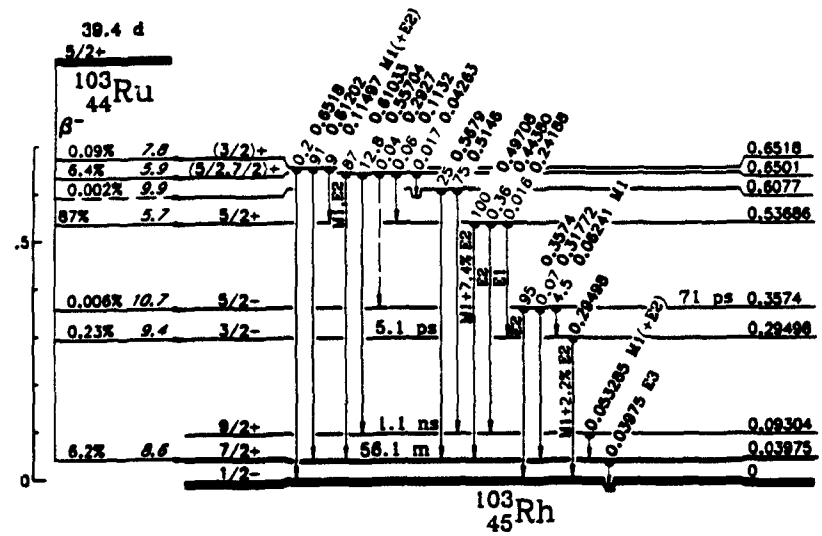

Figure A.3: Decay scheme for ^{103}Ru.
Adapted from Ref.[168].

B Appendix: SLOWPOKE-2 facility

The critical assembly architecture of the Dalhousie University SLOWPOKE-2 Reactor (DUSR) is illustrated in Figure B.1. The reduction in reactivity resulting from a build up of fission products as the ^{235}U is consumed, is compensated for by the addition of beryllium shim plates to the top of the core reflector (see Ref. [88]). The facility has five inner sites (located within the side Beryllium reflector) and three outer sites (within the water which surrounds the assembly). Table B.1 details the neutron flux characteristics within the inner and outer sites. These numbers were originally published in 1987, however, there has been no significant change up to the time of writing this thesis [169].

Parameters	Inner site	outer site
Maximum thermal flux [n/barn/sec]	$1.1x10^{-12}$	$5.4x10^{-13}$
Maximum fast flux [n/barn/sec]	$2.4x10^{-13}$	$2.4x10^{-14}$
Fast-to-thermal flux ratio	0.22	0.044
Variation in vertical homogeneity [%/cm]	~0.5	~0.5
Variation in radial homogeneity [%/cm]	~0.5	6

Table B.1: Composition and homogeneity of the DUSR neutron flux determined in 1987 after the installation of a big shim to the reactor core.
Adapted from Ref. [88].

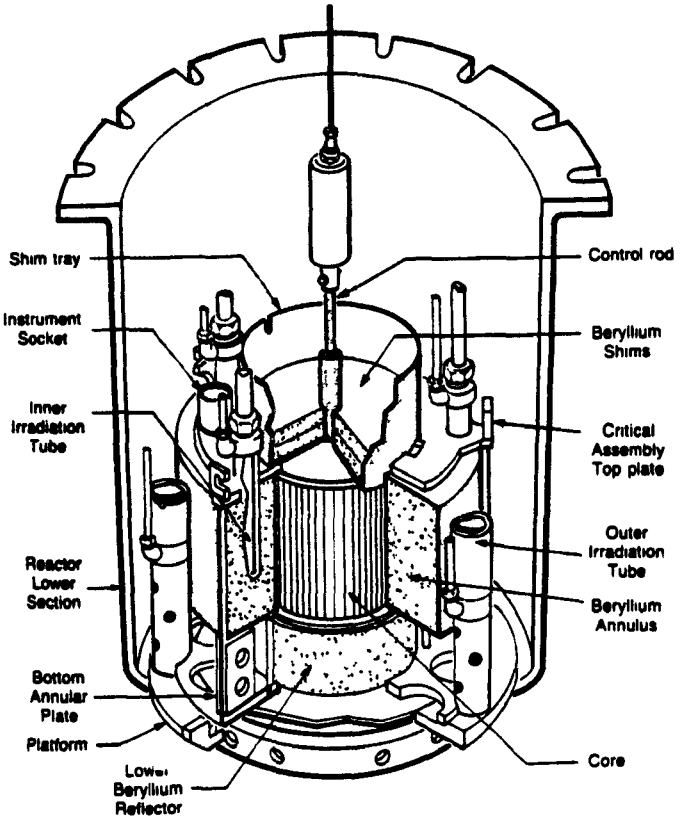

Figure B.1: Schematic of the SLOWPOKE-2 critical assembly (courtesy of the Atomic Energy of Canada Limited - Research Company). The assembly is submerged in water.

C Appendix: *In situ* source activity

In this appendix, details of the calculation of the expected activity, $\mathcal{A}$, from a radioactive substance formed (by neutron capture) at a constant rate are given. In this process, the number of radioactive atoms, N, is given by the differential equation:

$$dN/dt = Q - \lambda N, \tag{C.1}$$

where

$$Q = \sigma_c \Phi (m/A) \tag{C.2}$$

is the rate at which they are being produced via neutron capture. $\lambda = ln2/t_{1/2}$ is the decay rate of the radioactive isotope, σ is the neutron capture cross section for the parent isotope, Φ is the neutron flux, m is the sample mass and A is the atomic mass [1]. With the boundary condition,

$$N(0) = 0, \tag{C.3}$$

the solution to eqn (C.1) becomes

$$N(t) = (Q/\lambda)(1 - e^{-\lambda t}). \tag{C.4}$$

Since the activity of the radioactive isotope $\mathcal{A}(t) = \lambda N(t)$, eqns (C.2) and (C.4) yield,

$$\mathcal{A}(t)[Ci] = (2.7 \times 10^{-11})(\sigma_c \Phi (m/A))(1 - e^{-\lambda t}). \tag{C.5}$$

$$\left[\begin{array}{ll} \sigma_c & = \textit{thermal neutron cross section } [barns] \\ \Phi & = \textit{thermal neutron flux } [n/barn/sec] \\ m & = \textit{mass of parent isotope } [g] \\ A & = \textit{atomic mass of parent isotope } [g/atom] \\ \lambda & = \textit{decay rate of radioactive isotope } [/sec] \end{array}\right.$$

[1] m and A correspond to that of the particular isotope of interest within that sample.

As an example, the ^{64}Cu activity, $\mathcal{A}$, from a 10 min irradiation of a sample containing 50.0 mg of Cu (^{63}Cu is 69.2% *N.A.*),

$$\begin{cases} \sigma_c &= 4.42\ barns \\ \Phi &= 5.4 \times 10^{-13}\ n/barn/sec \\ m &= 0.692 \times 0.0500g\ =\ 0.0346\ g \\ A &= 62.93\ AMU\ =\ 1.045 \times 10^{-22}\ g/atom \\ \lambda &= 0.693/12.7hr\ =\ 1.516 \times 10^{-5}/sec \end{cases}$$

is 280 μCi.

References

[1] D. Shechtman, I. Blech, D. Gratias, and J.W. Cahn. *Phys. Rev. Lett.*, 53:1951, 1984.

[2] D.P. DiVincenzo and P.J. Steinhardt (eds.). *Quasicrystals: The State of the Art.* World Scientific, Singapore, 1991.

[3] A.I. Goldman and M. Widom. *Ann. Rev. Phys. Chem.*, 42:685, 1991.

[4] P. Guyot, P. Kramer, and M. de Boissieu. *Rep. Prog. Phys.*, 54:1373, 1991.

[5] K.F. Kelton. *Int. Mater. Rev.*, in press, 1992.

[6] C. Janot. *Quasicrystals: A Primer.* Oxford University Press, New York, 1992.

[7] A.I. Goldman and K.F. Kelton. *Rev. Mod. Phys.*, 65:213, 1993.

[8] K.F. Kelton, P.C. Gibbons, and A.I. Goldman (eds.). *Quasicrystals 4: Proceedings of the 4th International Conference on Quasicrystals (St. Louis).* North-Holland, Amsterdam, 1993.

[9] N. Wang, H. Chen, and K.H. Kuo. *Phys. Rev. Lett.*, 59:1010, 1987.

[10] W. Cao, H.Q. Ye, and K.H. Kuo. *Phys. Stat. Sol. (a)*, 107:511, 1988.

[11] N. Wang, K.K. Fung, and K.H. Kuo. *Appl. Phys. Lett.*, 52:2120, 1988.

[12] Z.M. Wang and K.H. Kuo. *Acta Cryst. A*, 44:857, 1988.

[13] Y. Ma, R. Wang, and K.H. Kuo. *Scripta Met.*, 22:1791, 1988.

[14] K.H. Kuo. *Materials Science Forum*, 22-24:131, 1987.

[15] P.A. Bancel, P.A. Heiney, P.W. Stephens, A.I. Goldman, and P.M. Horn. *Phys. Rev. Lett.*, 54:2422, 1985.

[16] L. Bendersky. *Phys. Rev. Lett.*, 55:1461, 1985.

[17] C.B. Shoemaker, D.A. Keszler, and D.P. Shoemaker. *Acta Cryst. B*, 45:13, 1989.

[18] K.K. Fung, C.Y. Yang, Y.Q. Zhou, J.G. Zhao, W.S. Zhan, and B.G. Shen. *Phys. Rev. Lett.*, 56:2060, 1986.

[19] C. Dong, B.G. Li, and K.H. Kuo. *J. Phys. F.: Metal Phys.*, 17:L189, 1987.

[20] X.Z. Li and K.H. Kuo. *Phil. Mag. Lett.*, 58:167, 1988.

[21] Y. Ma and E.A. Stern. *Phys. Rev. B*, 35:2678, 1987.

[22] L.X. He, Y.K. Wu, and K.H. Kuo. *J. Mater. Sci.*, 7:1284, 1988.

[23] H. Zhang and K.H. Kuo. *Scripta Met.*, 23:355, 1989.

[24] A.P. Tsai, A. Inoue, and T. Masumoto. *Mater. Trans., JIM*, 30:666, 1989.

[25] A.P. Tsai, A. Inoue, and T. Masumoto. *Mater. Trans., JIM*, 30:463, 1989.

[26] A.P. Tsai, A. Inoue, and T. Masumoto. *Phil. Mag. Lett.*, 64:163, 1991.

[27] C. Beeli, H.U. Nissen, and J. Robadey. *Phil. Mag. Lett.*, 63:87, 1991.

[28] T. Ishimasa, H.V. Nissen, and Y. Fukano. *Phil. Mag. A*, 58:835, 1988.

[29] H. Chen, D.X. Li, and K.H. Kuo. *Phys. Rev. Lett.*, 60:1645, 1988.

[30] A. Inoue, H.M. Kimura, and T. Masumoto. *J. Mater. Sci.*, 22:1758, 1987.

[31] H. Zhang, D.H. Wang, and K.H. Kuo. *Phys. Rev. B*, 37:6220, 1988.

[32] H.S. Chen, J.C. Phillips, P. Villars, A.R. Kortan, and A. Inoue. *Phys. Rev. B*, 35:9326, 1987.

[33] S.M. Anlage, B. Fultz, and K.M. Krishnan. *J. Mat. Res.*, 3:421, 1988.

[34] P.A. Bancel and P.A. Heiney. *Phys. Rev. B*, 33:7922, 1986.

[35] C. Janot and J.M. Dubois. *J. Phys. F: Metal Phys.*, 18:2303, 1988.

[36] P. Sainfort and B. Dubost. *J. Phys. (Paris)*, 47:C3–321, 1986.

[37] G.V.S. Sastry, V.V. Rao, P. Ramachandrarao, and T.R. Anantharaman. *Scripta Met.*, 20:191, 1986.

[38] K. F. Kelton, P.C. Gibbons, and P.N. Sabes. *Phys. Rev. B*, 38:7810, 1988.

[39] Z. Zhang, H.R. Ye, and K.H. Kuo. *Phil. Mag. A*, 52:L49, 1985.

[40] D. Bahadur, V. Srinivas, R.A. Dunlap, R.C. O'Handley, and M.E. McHenry. *Phil. Mag. B*, 60:871, 1989.

[41] C.L. Henley and V. Elser. *Phil. Mag. B*, 53:L59, 1986.

[42] N.K. Mukhopadhyay, N. Thangaraj, K. Chattopadhyay, and S. Ranganathan. *J. Mater. Res.*, 2:299, 1987.

[43] I.M. Reany and G.W. Lorimer. *Phil. Mag. Lett.*, 57:247, 1988.

[44] K.H. Kuo, C. Dong, D.S. Zhou, Y.X. Guo, Z.K. Hei, and D.X. Li. *Scripta Met.*, 20:1695, 1986.

[45] S.J. Poon, A.J. Drehmann, and K.R. Lawless. *Phys. Rev. Lett.*, 55:2324, 1985.

[46] W. Ohashi and F. Spaepen. *Nature*, 330:555, 1987.

[47] A.P. Tsai, A. Inoue, and T. Masumoto. *J. Mater. Sci. Lett.*, 7:322, 1988.

[48] A.P. Tsai, A. Inoue, and T. Masumoto. *Mater. Trans., JIM*, 29:521, 1988.

[49] Y. Yokoyama, A. Inoue, and T. Masumoto. *Mater. Trans., JIM*, 33:1012, 1992.

[50] A.P. Tsai, A. Inoue, and T. Masumoto. *Jpn J. Appl. Phys.*, 26:L1505, 1987.

[51] A.P. Tsai, A. Inoue, and T. Masumoto. *Jpn J. Appl. Phys.*, 27:L1587, 1988.

[52] A. P. Tsai, N. Kataoka, A. Inoue, and T. Masumoto. *Jpn. J. Appl. Phys.*, 29:L1696, 1990.

[53] T.-L. Ho. In K.J. Strandburg, editor, *Bond-Orientational Order in Condensed Matter Systems*, page 216, Springer-Verlag, New York, 1992.

[54] S.J. Poon. *Adv. Phys.*, 41:303, 1992.

[55] S.S. Kang and J.M. Dubois. *Phil. Mag. A*, 66:151, 1992.

[56] T. Shibuya, T. Hashimoto, and S. Takeuchi. *Jpn. J. Appl. Phys.*, 29:L349, 1990.

[57] L. Bresson and D. Gratias. *J. Non-Cryst. Solids*, 153/154:468, 1993.

[58] T. Klein, C. Berger, D. Mayou, and F. Cyrot- Lackmann. *Phys. Rev. Lett.*, 66:2907, 1991.

[59] D. Mayou, C. Berger, F. Cyrot-Lackmann, T. Klein, and P. Lanco. *Phys. Rev. Lett.*, in press, 1993.

[60] B.D. Biggs, S.J. Poon, and N.R. Munirathnam. *Phys. Rev. Lett.*, 65:2700, 1990.

[61] E. Belin. In P. Jena, S.N. Khanna, and B.K. Rao, editors, *Physics and Chemistry of Finite Systems: from Clusters to Crystals (NATO ASI Series C, vol 374)*, page 829, Klewer Academic Publishers, Dordrecht, 1992.

[62] A.P. Tsai, Y. Yokoyama, A. Inoue, and T. Masumoto. In P. Jena, S.N. Khanna, and B.K. Rao, editors, *Physics and Chemistry of Finite Systems*, page 177, Kluwer Academic Publishers, Dordrecht, 1992.

[63] W.B. Pearson. *The Crystal Chemistry and Physics of Metals and Alloys.* Wiley, New York, 1972.

[64] S.E. Burkov, T. Timusk, and N.W. Ashcroft. *J. Phys.: Condens. Matter*, 4:9447, 1992.

[65] P.J. Schultz and K.G. Lynn. *Rev. Mod. Phys.*, 60:701, 1988.

[66] W. Brandt. In A.T. Stewart and L.O. Roellig, editors, *Positron Annihilation: proceedings of the 1st International Conference on Positron Annihilation, Detroit*, page 155, Academic Press, New York/London, 1965.

[67] I.K. MacKenzie, T.L. Khoo, A.B. McDonald, and B.T.A. McKee. *Phys. Rev. Lett.*, 19:946, 1967.

[68] B. Bergersen and M.J. Stott. *Solid State Commun.*, 7:1203, 1969.

[69] D.C. Connors and R.N. West. *Phys. Lett. A*, 30:24, 1969.

[70] A. Janner and T. Janssen. *Physica A*, 99:47, 1979.

[71] P. Bak. *Phys. Rev. Lett.*, 54:1517, 1985.

[72] A. Katz and M. Duneau. *Phys. Rev. Lett.*, 54:2688, 1985.

[73] C. Janot. *J. Non-Cryst. Solids*, 156-158:852, 1993.

[74] C.L. Henley. In D.P. DiVincenzo and P.J. Steinhardt, editors, *Quasicrystals, The State of the Art*, page 429, World Scientific, Singapore, 1991.

[75] P.W. Stephens and A.I. Goldman. *Phys. Rev. Lett.*, 56:1168, 1986.

[76] J. Devaud-Rzepski, M. Cornier-Quiquandon, and D. Gratias. In , editor, *Third Int. Meeting on Quasicrystals: Quasicrystals and Incommensurate Structures*, page 498, World Scientific, Singapore, 1989.

[77] M. Wollgarten, D. Gratias, Z. Zhang, and K. Urban. *Phil. Mag. A*, 64:819, 1991.

[78] M. Wollgarten, Z. Zhang, and K. Urban. *Phil. Mag. Lett.*, 65:1, 1992.

[79] Z. Zhang and Y. Zhuang. *Phil. Mag. Lett.*, 65:203, 1992.

[80] D.P. Yu, W. Staiger, and M. Kleman. *J. Non-Cryst. Solids*, 153/154:453, 1993.

[81] K. Urban, M. Wollgarten, D. Gratias, and Z. Zhang. *J. Non-Cryst. Solids*, 153/154:519, 1993.

[82] R. Wang and M.X. Dai. *Phys. Rev. B*, 47:15326, 1993.

[83] D. Levine, T.C. Lubensky, S. Ostlund, S. Ramaswamy, P.J. Steinhardt, and J. Toner. *Phys. Rev. Lett.*, 54:1520, 1985.

[84] J.E.S. Socolar, T.C. Lubensky, and P.J. Steinhardt. *Phys. Rev. B*, 34:3345, 1986.

[85] M. Kleman. *J. Phys. (Paris) I*, 2:69, 1992.

[86] D. Shechtman and I. Blech. *Met. Trans. A*, 16:1005, 1985.

[87] I.K. MacKenzie. In W. Brandt and A. Dupasquier, editors, *Positron Solid-State Physics*, page 196, North-Holland, Amsterdam, 1983.

[88] D.E. Ryan, A. Chatt, and J. Holzbecher. *Analytica Chimica Acta*, 200:89, 1987.

[89] I.K. MacKenzie and J. Fabian. *Nuovo Cimento B*, 58:162, 1980.

[90] D.W. Marquardt. *J. Soc. Indust. Appl. Math.*, 11:431, 1963.

[91] I.K. MacKenzie, J.A. Eady, and R.R. Gingerich. *Phys. Lett. A*, 33:279, 1970.

[92] J.L. Campbell. *Appl. Phys.*, 13:365, 1977.

[93] P.J. Schultz, R.W. Ollerhead, P.C. Lichtenberger, B.G. Nickel, J.R. MacDonald, and I.K. MacKenzie. *Can. J. Phys.*, 59:325, 1981.

[94] R.W. Siegel. *Ann. Rev. Mater. Sci.*, 10:393, 1980.

[95] H.E. Schaefer, W. Stuck, and et.al. In C. Abromeit and H. Wollenberger, editors, *Vacancies and Interstitials in Metals and Alloys*, page 117, Trans. Tech. Publ., Aedermannsdrf, 1987.

[96] H. Fukushima and M. Doyama. *J. Phys. F: Metal Phys.*, 6:677, 1976.

[97] P. Rice-Evans, T. Hlaing, and D.B. Rees. *J. Phys. F: Metal Phys.*, 6:1079, 1976.

[98] A.S. Berger, S.T. Ockers, and R.W. Siegel. *J. Phys. F: Metal Phys.*, 9:1023, 1979.

[99] M.J. Fluss, L.C. Smedskjaer, R.W. Siegel, D.G. Legnini, and M.K. Chason. *J. Phys. F: Metal Phys.*, 10:1763, 1980.

[100] T.E. Jackman, P.C. Lichtenberger, and C.W. Schulte. *Appl. Phys.*, 5:259, 1974.

[101] S. Dannefaer and D.P. Kerr. *Nucl. Instr. Methods*, 131:119, 1975.

[102] P. Verkerk. *Comp. Phys. Comm.*, 25:325, 1982.

[103] J.P. Schaffer, E.J. Shaughnessy, and P.L. Jones. *Nucl. Instr. Met. Phys. Res. B*, 5:75, 1984.

[104] J.P. Schaffer and P.L. Jones. *J. Phys. F: Met. Phys.*, 16:1885, 1986.

[105] D.T. Britton and P.C. Rice-Evans. *Phys. Stat. Sol. (b)*, 147:89, 1988.

[106] N. Shiotani, N. Sakai, H. Sekizawa, and T. Mizoguchi. *J. Phys. Soc. Japan*, 50:828, 1981.

[107] G. Dlubek and [illegible] Gerber. *Phys. Stat. Sol. (a)*, [illegible]81, 1990.

[108] P. Kirkegaard and M. Eldrup. *Comput. Phys. Commun.*, 3:240, 1972.

[109] P. Kirkegaard and M Eldrup. *Comput. Phys. Commun.*, 7:401, 1974.

[110] P. Kirkegaard, M. Eldrup, O.E. Mogensen, and N.J. Pedersen. *Comput. Phys. Commun.*, 23:307, 1981.

[111] C. Hidalgo, N. de Diego, and P. Moser. *Appl. Phys. A*, 40:25, 1986.

[112] A. Seeger, F. Banhart, and W. Bauer. In L. Dorikens-Vanpraet, M. Dorikens, and D. Segers, editors, *Positron Annihilation*, page 275, World Scientific, Singapore, 1989.

[113] R.A. Dunlap, D.W. Lawther, and R.H. March. *J. Phys. F: Met. Phys.*, 17:L39, 1987.

[114] M.K. Sanyal, P.M.G. Nambissan, R. Chidambaram, and P. Sen. *J. Phys.: Condens. Matter*, 1:3733, 1989.

[115] T. Kizuka, I. Kanazawa, Y. Sakurai, S. Nanao, H. Murakami, and T. Iwashita. *Phys. Rev. B*, 40:796, 1989.

[116] R. Chidambaram, M.K. Sanyal, P.M.G. Nambissan, and P. Sen. *J. Phys.: Condens. Matter*, 2:251, 1990.

[117] R. Chidambaram, M.K. Sanyal, P.M.G. Nambissan, and P. Sen. *Bull. Am. Phys. Soc.*, 35:331, 1990.

[118] T. Ohata, I. Kanazawa, T. Iwashita, K. Kishi, and S. Takeuchi. *Phys. Rev. B*, 42:6730, 1990.

[119] I. Kanazawa, T. Kizuka, M. Ohata, Y. Sakurai, S. Nanao, and T. Iwashita. *J. Non-Cryst. Solids*, 117/118:793, 1990.

[120] D.W. Lawther, G. Beydaghyan, and R.A. Dunlap. *J. Phys.: Condens. Matter*, 2:6239, 1990.

[121] R. Chidambaram, M.K. Sanyal, P.M.G. Nambissan, and P. Sen. *J. Phys.: Condens. Matter*, 2:9941, 1990.

[122] R.H. Howell, C. Berger, F. Solal, Y. Calvayrac, and P.E.A. Turchi. *Mater. Sci. Forum*, 105-110:651, 1992.

[123] D. Shi, L.Y. Xiong, and W. Deng. *Mater. Sci. Forum*, 105-110:829, 1992.

[124] I. Kanazawa, T. Iwasita, T. Ohata, S. Nanao, and S. Takeuchi. *Mater Sci. Forum*, 105-110:1093, 1992.

[125] K. Kristiakova, S. Makinen, J. Kristiak, and D. Janickovic. *Mater. Sci. Forum*, 105-110:1113, 1992.

[126] Y. Nakao, T. Shibuya, S. Takeuchi, W. Liu, X.-S. Li, and S. Berko. *Phys. Rev. B*, 46:3108, 1992.

[127] D.W. Lawther and R.A. Dunlap. *J. Non-Cryst. Solids*, 153/154:611, 1993.

[128] D.W. Lawther and R.A. Dunlap. *Key Engineering Matrials*, 81/82:95, 1993.

[129] R. Chidambaram, M.K. Sanyal, V.S. Raghunathan, P.M.G. Nambissan, and P. Sen. *Phys. Rev. B*, in press, 1993.

[130] I. Kanazawa, Chi. Nakayama, J. Takahashi, T. Ohata, T. Iwashita, and T. Kizuka. *Phy. Rev. B*, submitted, 1993.

[131] D.W. Lawther and R.A. Dunlap. *Phys. Rev. B*, submitted, 1993.

[132] D.W. Lawther, R.A. Dunlap, V. Srinivas, D.J. Lloyd, and S. Jha. *Hyperf. Interact.*, 60:785, 1990.

[133] S.K. Sikka, Surinder M. Sharma, and R. Chidambaram. *Phys. Rev. B*, 47:2878, 1993.

[134] E.E. Cherkashin, P.I. Kripyakevich, and G.I. Oleksiv. *Kristallografiya*, 8:846, 1963.

[135] A.P. Tsai, A. Inoue, and T. Masumoto. *J. Mater. Sci. Lett.*, 6:1403, 1987.

[136] M. Cornier-Quiquandon, A. Quivy, S. Lefebvre, E. Elkaim, G. Heger, A. Katz, and D. Gratias. *Phys. Rev. B*, 44:2071, 1991.

[137] Y. Calvayrac, A. Quivy, M. Bessiere, S. Lefebvre, M. Cornier-Quiquandon, and D. Gratias. *J. Phys. (Paris)*, 51:417, 1990.

[138] R.A. Dunlap and D.W. Lawther. *Mater. Sci. Eng. R*, 10:141, 1993.

[139] M. Eibschutz, M.E. Lines, H.S. Chen, and F.A. Thiel. *Phys. Rev. B*, 46:491, 1992.

[140] A. Shastri, F. Borsa, A.I. Goldman, J.E. Shield, and D.R. Torgeson *J. Non-Cryst. Solids*, 153/154:347, 1993.

[141] E. H. du Marchie van Voorthuysen, P.J.M. Smulders, R.D. Werkman, J.L. de Boer, and S. van Smaalen. *Phys. Rev. B*, 45:9667, 1992.

[142] M. Bessiere, A. Quivy, S. Lefebvre, J. Devaud-Rzepski, and Y. Calvayrac. *J. Phys. (Paris) I*, 1:1823, 1991.

[143] F.S. Pierce, P.A. Bancel, B.D. Biggs, Q. Guo, and S.J. Poon. *Phys. Rev. B*, 47:5670, 1993.

[144] P. Lindqvist, C. Berger, T. Klein, P. Lanco, F. Cyrot-Lackmann, and Y. Calvayrac. *Phys. Rev. B*, 48:630, 1993.

[145] A. Sadoc, E. Belin, Z. Dankhazi, and A.M. Flank. *J. Non-Cryst. Solids*, 153/154:338, 1993.

[146] E. Belin and Z. Danhkazi. *J. Non-Cryst. Solids*, 153/154:298, 1993.

[147] E. Belin, Z. Dankhazi, and A. Sadoc. *J. Non-Cryst. Solids*, 156-158:896, 1993.

[148] Z.M. Stadnik and G. Stroink. *J. Non-Cryst. Solids*, 156-158:891, 1993.

[149] S. Matsuo, T. Ishimasa, M. Mori, and H. Nakano. *J. Phys.: Condens. Matter*, 4:10053, 1992.

[150] U. Koster, W. Liu, H. Liebertz, and M. Michel. *J. Non-Cryst. Solids*, 153/154:446, 1993.

[151] D. Gratias, Y. Calvayrac, J. Devaud-Rzepski, F. Faudot, M. Harmelin, A. Quivy, and P.A. Bancel. *J. Non-Cryst. Solids*, 153/154:482, 1993.

[152] T. Ishimasa and M. Mori. *Phil. Mag. Lett.*, 62:357, 1990.

[153] M. Mori, S. Matsuo, T. Ishimasa, T. Matsuura, K. Kamiya, H. Inokuchi, and T. Matsukawa. *J. Phys.: Condens. Matter*, 3:767, 1991.

[154] R.M. Nieminen and J. Laakkonnen. *Appl. Phys.*, 20:181, 1979.

[155] M.J. Puska and R.M. Nieminen. *J. Phys. F: Met. Phys.*, 13:333, 1983.

[156] A.P. Tsai, A. Inoue, and T. Masumoto. *Sci. Rep. Ritu A*, 36:99, 1991.

[157] L. Pauling. *Phys. Rev.*, 54:899, 1938.

[158] A. Seeger and F. Banhart. *Phys. Stat. Sol. (a)*, 102:171, 1987.

[159] A. Baranowski and E. Debowska. *Appl. Phys.*, 51:23, 1990.

[160] F. Denoyer, G. Heger, M. Lambert, M. Audier, and P. Guyot. *J. Phys. (Paris)*, 51:651, 1990.

[161] T. Motsch, F. Denoyer, P. Launois, and M. Lambert. *J. Phys. (Paris) I*, 2:861, 1992.

[162] M. Audier, Y. Brechet, M. deBoissieu, P. Guyot, C. Janot, and J.M. Dubois. *Phil. Mag. B*, 63:1375, 1991.

[163] R.M. Nieminen. In W. Brandt and A. Dupasquier, editors, *Positron Solid-State Physics*, page 359, North-Holland, Amsterdam, 1983.

[164] G. Coddens, R. Bellissent, Y. Calvayrac, and J.P. Ambroise. *Europhys. Lett.*, 16:271, 1991.

[165] G. Coddens and R. Bellissent. *J. Non-Cryst. Solids*, 153/154:557, 1993.

[166] G. Coddens, C. Soustelle, R. Bellissent, and Y. Calvayrac. *Europhys. Lett.*, 23:33, 1993.

[167] P. Hautojarvi, J. Heinio, M. Manninen, and R. Nieminen. *Phil. Mag.*, 35:973, 1977.

[168] E. Browne, J.M. Dairiki, R.E. Doebler, A.A. Shihab-Eldin, L.J. Jardine, J.K. Tuli, and A.B. Buyrn. *Table of Isotopes, 7th Edition (C.M. Lederer and V.S. Shirley (eds.))*. Wiley-Interscience, New York, 1978.

[169] J. Holzbecher. *private communication*, 1993.